



HAL
open science

Solving transient coupled conductive and radiative transfers in porous media with a Monte Carlo Method: Characterization of thermal conductivity of foams using a numerical Flash Method

Morgan Sans, Olivier Farges, Vincent Schick, Gilles Parent

► To cite this version:

Morgan Sans, Olivier Farges, Vincent Schick, Gilles Parent. Solving transient coupled conductive and radiative transfers in porous media with a Monte Carlo Method: Characterization of thermal conductivity of foams using a numerical Flash Method. *International Journal of Thermal Sciences*, 2022, 179, pp.107656. 10.1016/j.ijthermalsci.2022.107656 . hal-03681436v1

HAL Id: hal-03681436

<https://hal.science/hal-03681436v1>

Submitted on 1 Jun 2022 (v1), last revised 2 Jun 2022 (v2)

HAL is a multi-disciplinary open access archive for the deposit and dissemination of scientific research documents, whether they are published or not. The documents may come from teaching and research institutions in France or abroad, or from public or private research centers.

L'archive ouverte pluridisciplinaire **HAL**, est destinée au dépôt et à la diffusion de documents scientifiques de niveau recherche, publiés ou non, émanant des établissements d'enseignement et de recherche français ou étrangers, des laboratoires publics ou privés.

1 Solving transient coupled conductive and radiative transfers in porous media
2 with a Monte Carlo Method: characterization of thermal conductivity of foams
3 using a numerical Flash method.

4 Morgan Sans^a, Olivier Farges^a, Vincent Schick^a, Gilles Parent^{a,*}

5 ^aUniversité de Lorraine, CNRS, LEMTA, F-54000 Nancy, France

6 **Abstract**

This paper presents a single Monte-Carlo algorithm used to solve transient conductive and radiative heat transfers in three-dimensional porous media. The complete methodology presented step by step herein enables practical and efficient study of geometrical and multiphysical complexities. The code was validated against results obtained by commercial software, analytical and semi-analytical solutions. Computation times were found to be greatly reduced when radiative transfer is predominant compared with those obtained using a deterministic solver. This kind of approach allows a probe calculation in the frame of linear thermal transfers and is well suited for the numerical characterization of heterogeneous media. In this work a numerical flash method was reproduced and enabled us to evaluate the effective total conductivity of the equivalent homogenized medium. The influence of various parameters such as porosity, size of the unit cell, bulk conductivity of the solid phase, reference temperature and emissivity was studied for a stack of Kelvin cells. This tool enables the parametric investigation of geometric and thermal properties. The results are in good agreement with those of the literature.

7 *Keywords:* Monte-Carlo Method, Heat conduction, Thermal radiation, Flash Method, Equivalent thermal
8 conductivity, Porous media

9 **1. Introduction**

10 Ceramic and metallic foams are commonly used in many engineering applications because of their interesting
11 thermal, mechanical and optical properties[1]. Improved manufacturing processes enable the production of porous
12 media with a very wide range of structural parameters such as porosity, cell size distribution, geometries or materials
13 used. These can thus be designed and used for several applications such as catalysis, volumetric solar absorbers,
14 insulators, heat exchangers or gas-phase heat recovery. The foam structural and thermal parameters play a key role
15 in the efficiency of the studied systems because of the coupling between the different physical phenomena involved
16 such as conduction in the fluid/solid phase, convection, transport, radiation or chemical reaction. Their optimization
17 necessarily requires better knowledge of the link between the porous heterogeneous medium and the coupled heat
18 transfer mechanisms and this can be achieved by using numerical and experimental tools.

19
20 Nowadays, combined heat transfers can be solved directly on complex geometry at the sample scale, i.e. at a scale
21 equal to a few (dozen of) size of pores, but this becomes difficult at the scale of the system itself. Therefore, it is very
22 common for the thermal problem to be simplified by considering foam as a homogeneous medium with equivalent
23 thermal properties, which represents the overall thermal transport through the medium and has to be characterized.
24 In this framework, a unique Equivalent Thermal Conductivity (ETC), which can include conduction, convection and
25 radiation has been widely considered. Interested readers can refer to [2], which gives a broad overview of the studied
26 geometries in different scopes of validity. Analytical solutions or numerical tools have been provided for the simplest

*Corresponding author.

Email address: gilles.parent@univ-lorraine.fr (Gilles Parent)

Nomenclature

Greek Symbols

α	Thermal diffusivity ($\text{m}^2 \cdot \text{s}^{-1}$)
δ	Space jump (m)
δ_b	Space jump at the boundary (m)
δ_w	Space jump to the boundary (m)
ϵ	Emissivity (–)
λ_s	Bulk thermal conductivity ($\text{W} \cdot \text{m}^{-1} \cdot \text{K}^{-1}$)
Φ	Transient heat excitation ($\text{W} \cdot \text{m}^{-2}$)
ρ'	directional-hemispherical reflectivity (–)
σ	Stefan-Boltzmann constant ($5.67 \times 10^{-8} \text{W} \cdot \text{m}^{-2} \cdot \text{K}^{-4}$)
τ	Time decrement (s)
θ	Polar angle (rad)
θ_i	i^{th} realization of the MC algorithm (K)
ε	Porosity (–)
φ	Azimuthal angle (rad)

Latin Symbols

\mathcal{D}_s	Domain (–)
\mathcal{E}	Expectation of a random variable (–)
\mathcal{H}	Heaviside function (–)
\mathcal{H}	Heaviside step function (–)
$\partial\mathcal{D}_\Phi$	Contour with heat excitation (–)
$\partial\mathcal{D}_{fs}$	Fluid/solid contour (diffusive wall) (–)
$\partial\mathcal{D}_p$	Contour with periodic condition (–)
$\partial\mathcal{D}_{rf}$	Contour of the rear face (–)
$\partial\mathcal{D}_s$	Contour (–)
\mathbf{n}	Unitary outward normal vector (–)
\mathbf{u}	Direction of conductive propagation (–)
\mathbf{v}	Direction of incident intensity (–)
\mathbf{v}_r	Direction of reflected intensity (–)
\mathbf{x}	Location (–)
Bi	Radiative Biot number (–)
D_{cell}	Size of a unit cell (m)
F	Cumulative density function of the azimuthal angle (–)
G	Cumulative density function of the polar angle (–)
H	Cumulative density function of the time (–)
h_{rad}	Radiative exchange coefficient ($\text{W} \cdot \text{m}^{-2} \cdot \text{K}^{-1}$)
I	Radiant intensity ($\text{W} \cdot \text{m}^{-2} \cdot \text{sr}^{-1}$)
i	i^{th} realization of the MC algorithm (–)
j	j^{th} interaction with the excited face (–)

J_i	Number of excitation with the excited surface of the i^{th} realization (–)
N_{mc}	Number of Monte Carlo realization (–)
p_X	probability density function of a random variable X (–)
p_{cond}	Probability of following a conductive path (–)
p_{rad}	Probability of following a radiative path (–)
Q	Constant heat flux deposited ($\text{W} \cdot \text{m}^{-2}$)
S	Surface (m^2)
S_i	Source term of the i^{th} realization (K)
T	Temperature (K)
t	Time (s)
T_{cold}	Imposed cold temperature (K)
T_{hot}	Imposed hot temperature (K)
T_{rad}	Averaged radiative temperature (K)
T_{ref}	Reference temperature (K)

Subscripts

Γ	Relating to the space of the paths (–)
γ	Relating to a given path (–)
I	Relating to the initial condition (–)
b	Relating to the boundary (–)
cond	Relating to conductive heat transfer (–)
eff	Relating to effective heat transfer (–)
eq	Relating to total equivalent heat transfer (–)
i	Relating to the intersection (–)
max	Relating to the maximum value (–)
obs	Relating to the probe computation location (–)
rad	Relating to radiative heat transfer (–)
rf	Relating to the rear face (–)

Superscripts

*	Relating to dimensionless quantities (–)
0	Blackbody (–)

Other Symbols

\bar{X}	Estimator of the quantity X (–)
-----------	-----------------------------------

27 geometries [3] while numerical or experimental characterization procedures have been developed to study 3D complex
 28 porous geometries. The thermal behavior of metallic foams at ambient temperature were studied by Coquard and Bail-

lis [4] or by R. Wulf et al. [5] who used a numerical hot guarded plate method from tomographic images. Zhao et al. [6], Fend et al.[7] and Coquard et al. [8] used respectively an experimental guarded hot plane, a transient plan source and a flash method. Such studies can be used to explore the validity of the theoretical models described above, validate employed characterization procedures and highlight the main thermal or geometrical properties in heat transport.

Ceramic and metallic foams are particularly interesting for high-temperature applications in which radiation transfer plays a major role. The description of the radiative behavior in such media through the identification of equivalent optical properties has mostly been studied independently of the other modes of heat transport. Authors like Tancrez and Taine [9], Guévelou et al [10] or Loretz et al. [11] proposed numerical methods based on ray-tracing approaches and provided correlations from tomographic images while authors like Hendricks and Howell [12] or Baillis et al.[13] performed a spectral estimation of equivalent radiative properties from spectrometer measurements. Characterization following an entirely numerical procedure requires efficient modelling of the coupled thermal transfers directly on the complex and 3D heterogeneous medium. Solving this problem can remain quite tricky and time-consuming because of the different nature of the two modes of heat transfer. Indeed, sufficiently finely resolved and realistic geometry and optimized solvers for each of the transport modes are required to achieve this. To our knowledge, very few studies have focused on the numerical identification of equivalent properties of foams with coupled conductive and radiative transfer. Some authors like Mendes et al. [14] have proposed using a numerical hot guarded plate applied to metallic foams at high temperature and demonstrated the limits of using the Rosseland approximation to describe the equivalent radiative conductivity. Subsequently, these same authors developed a complete numerical study [14] to determine the possible bias generated by simplified radiative modeling of the medium (heterogeneous, homogeneous, Rosseland...). Empirical laws were then provided to make modeling these heterogeneous environments easier. Very recently, Vignoles and Ortona [15] proposed an original stochastic method to model both conduction and radiation in ceramic/metallic foams and fibers and identified total equivalent properties.

Experimental measurements of the conductivity of foams at high temperature are not common at all. The characterization procedure requires the use of a fast and accurate coupled model. Zhao et al. [6], Coquard and Baillis [16] and Mendes et al. [17] used the method involving a hot guarded plate while Coquard et al. [18] used the hot-wire to study coupling heat transfers in expanded polystyrene foams. Niezgodna et al.[19] applied the flash method to the study of a silica aerogel and other thermal insulators such as low density foams. However, due to a lack of sensitivity or to correlations between parameters, the identification of equivalent radiative properties was difficult and was performed separately. For the very first time, Coquard et al.[8] simultaneously characterized an equivalent conductivity and equivalent absorbing and scattering coefficients for metallic and ceramic foams (Zirconia, FeCr alloy, Mullite and NiCrAl) over a temperature range between 296 K and 673 K. The authors of the present paper recently reported this kind of characterization at temperatures up to 1000 K applied to SiC and SiSiC foams taking into account a wide variety of influential parameters such as the geometry of cells, pore diameter, bulk conductivity, the reference temperature and so on [20]. Nevertheless, this kind of experimental characterization is always time-consuming and costly, especially when aiming high temperatures. Moreover, the large number of possible combinations of intrinsic parameters makes a systemic parametric exploration difficult as this requires the right samples to be available. A numerical approach is thus necessary to assist with experimental characterization and anticipate needs.

As explained above, the numerical resolution of coupled heat transfers directly on complex geometry remains tricky and requires efficient numerical tools. To our knowledge, deterministic methods are commonly used such as the Finite Element Method (FEM) for conduction and the Discrete Ordinate Method for radiation [14, 5, 21, 22]. Recently, Fournier et al.[23] suggested the idea of solving multi-physical phenomena with a single Monte-Carlo algorithm. They also showed that this kind of algorithm can be constructed if the set of considered equations can be written as a Fredholm equation of the second kind corresponding to the linear heat transfer framework. Based on an integral formulation, a recursive (backward in time) algorithm computes the temperature at a given time and at a given location (probe calculation) of a complex 3D geometry. The different heat transfer modes are solved at once so there is no need to couple two independent solvers. As this method requires only a surface mesh, it is very practical to use and convenient for dealing with geometric and multiphysical complexities. Moreover, coupling this with tools developed by the image synthesis community (such as hierarchical grids) means performance levels can be increased by reducing computation times and through a demonstrated insensitivity to the mesh refinement [24]. Caliot et al. [25] applied

81 this algorithm in a stationary case involving a structured foam made of Kelvin cells. This approach has been validated
 82 for conductive and radiative transfers by comparison with a deterministic method. Ibarrart et al.[26] extended this
 83 to consider coupled conductive, advective and radiative heat transfers while Penazzi et al. [27] studied the case of a
 84 semi-transparent medium. Assuming the linearity of heat transfers is a not limiting factor because only a small in-
 85 crease of the equilibrium temperature of the medium is required in most of the characterization methods, including the
 86 flash method. Moreover, recent studies have shown that solutions can be found to manage nonlinear problems [28].
 87 Finally, the Monte-Carlo algorithm and in particular its probe calculation aspect as proposed by Fournier et al.[23]
 88 appears highly suitable to use in the field of thermal characterization as it provides the solution to the direct model on
 89 the complex geometry. In this paper, we propose to apply the algorithm to the particular case of the flash method and
 90 to demonstrate the high potential of this approach for the study of coupled transfers in a heterogeneous medium.

91
 92 In the following, we shall first describe the thermal problem and governing equations concerned by our work.
 93 Secondly, we shall go on to describe the generic principle of the Monte-Carlo algorithm, which allows geometrical
 94 and multiphysical complexities to be dealt with in a very practical and efficient way. The complete methodology and
 95 the particular configuration of the flash method are detailed. Compared to previous studies [25, 26, 27], the present
 96 problem requires a transient solution. Thus, a validation case is provided for a 3D geometry which could be useful as
 97 a benchmark case for further algorithmic improvements. A comparison with a calculation performed by a commercial
 98 software based on deterministic methods also helps highlight the interests of our approach. Next the construction of
 99 the geometry of foams is presented and the identification procedure based on the numerically obtained thermograms
 100 is briefly described. Finally, a parametric study is presented. The influence of main parameters is studied including
 101 porosity, size of the cells, bulk conductivity of the foam struts, the bulk emissivity and the reference temperature on
 102 the total heat transfer.

103 2. METHODS

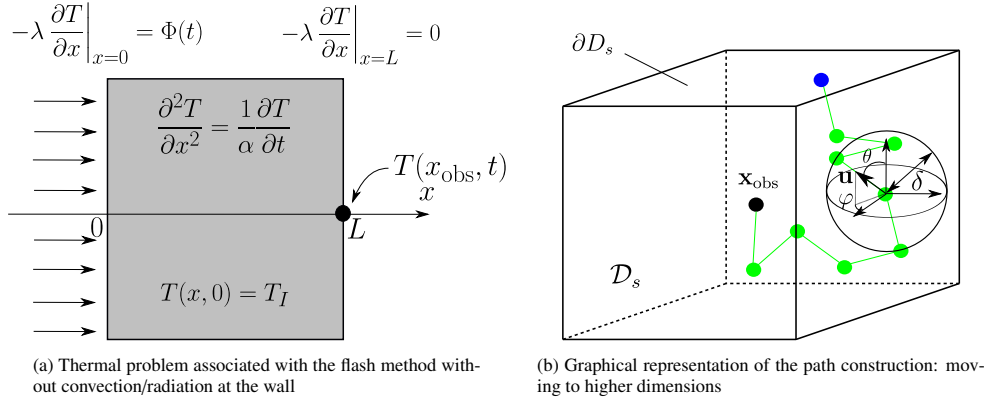


Figure 1: Principle of the flash method and walking technique for conduction

104 As explained previously, the flash method is an efficient method for measuring the total equivalent conductivity
 105 of a semi-transparent medium. In addition, the transient nature of this characterization method means it is possible
 106 to separate different contributions and the authors successfully achieved this to characterize experimentally silicon
 107 carbide foams at high temperature [20]. The idea of the present paper is to replace an experimental flash method
 108 by an entirely numerical one. Although the guarded hot plate or hot wire methods appear as references and are also
 109 well suited for such an identification of thermal properties, only the flash method is discussed here to benefit from the
 110 previous experience developed and allow comparison. However, there is no limit to the extension of the methodology
 111 described in this section to other characterization techniques.

112 In the experimental flash method (cf. fig. 1(a)), a sample at thermal equilibrium T_I is excited with a short duration
 113 heat flux $\Phi(t)$ on its front face. The transient evolution of the mean surface temperature of the rear face $T(\mathbf{x}_{\text{obs}}, t)$ is

114 measured with an infrared camera. It is common to place the sample between two soleplates or to cover each face
 115 with a black coating [8, 20] Here this is necessary because of the semi-transparent nature of the sample and because of
 116 the experimental configuration used. The first soleplate absorbs the incident radiative heat flux and avoids the direct
 117 transmission of the laser excitation to the detector. The second is useful to avoid measuring volumetric emission.
 118 This means that a proper spatially averaged temperature can be measured. Finally, the porous medium is considered
 119 under vacuum, such that no natural convection or conduction through the fluid phase can occur. This choice was only
 120 made to isolate and identify conduction through the solid phase but no experimental or numerical limitations prevent
 121 such study of the influence of the fluid phase. After a presentation of the context of the study, the following section is
 122 dedicated to the description of the methodology used to provide the coupled direct model describing the heat transfer
 123 through the heterogeneous medium.

124 2.1. Monte-Carlo Method: General case

125 Fundamentally, the Monte Carlo (MC) method is a method that estimates integrals (and discrete sums) by inter-
 126 preting them as expectations. Any quantity that can be expressed in an integral form can be estimated using a MC
 127 algorithm, including differential problems that are initially formulated outside the framework of stochastic processes
 128 [29, 30]. In this paper, our work aimed to compute the temperature at location \mathbf{x}_{obs} and at time t , by following a
 129 large number of paths crossing the complex geometry. The temperature $T(\mathbf{x}_{\text{obs}}, t)$ is then the expectation of a random
 130 variable $\Theta(\mathbf{x}_{\text{obs}}, t)$:

$$\bar{T}(\mathbf{x}_{\text{obs}}, t) = \mathcal{E}[\Theta(\mathbf{x}_{\text{obs}}, t)] \approx \frac{1}{N_{\text{mc}}} \sum_{i=1}^{N_{\text{mc}}} \theta_i \quad (1)$$

131 with $\bar{T}(\mathbf{x}_{\text{obs}}, t)$ the Monte-Carlo estimator of $T(\mathbf{x}_{\text{obs}}, t)$, Θ a random variable and θ_i the i^{th} realization of this variable,
 132 which is determined from the i^{th} path inside the calculation domain. A path starts at the location \mathbf{x}_{obs} and at the time
 133 t where and when the temperature needs to be computed. A path stops when a known temperature such as the initial
 134 condition or a Dirichlet boundary condition is reached. The achieved temperature is retained as the weight of the i^{th}
 135 realization of the algorithm.

136 2.2. Monte-Carlo Method: Conductive path

137 Concerning the conduction, the transient Energy Balance Equation (EBE) is:

$$\frac{\partial T}{\partial t} = \alpha \nabla^2 T \quad \forall \mathbf{x} \in \mathcal{D}_s \quad (2)$$

138 One way to solve the given thermal problem is to use the finite difference method. In the case of a unidirectional
 139 problem, using an explicit Euler scheme (order 1) to approximate the time derivative, and a centered scheme (order 2)
 140 for the spatial derivative, the EBE (cf. eq. (1)) becomes :

$$\frac{T(x, t) - T(x, t - \tau)}{\tau} = \frac{\alpha}{\delta^2} [T(x + \delta, t - \tau) - 2T(x, t - \tau) + T(x - \delta, t - \tau)] \quad (3)$$

141 with δ the spatial discretization step and τ the temporal discretization step. The temperature at position x and time
 142 t is thus expressed as:

$$T(x, t) = \mu T(x + \delta, t - \tau) + (1 - 2\mu)T(x, t - \tau) + \mu T(x - \delta, t - \tau) \quad (4)$$

143 with $\mu = \alpha\tau/\delta^2$. For this example, the Courant-Friedrichs-Lewis (CFL) condition requires $\mu \leq 1/2$ for the explicit
 144 scheme to be stable. Following this condition, eq. (4) allows a probabilistic interpretation and is used to construct
 145 propagation paths:

$$T(x, t) = p_r T(x + \delta, t - \tau) + p_c T(x, t - \tau) + p_l T(x - \delta, t - \tau) \quad (5)$$

146 It is then possible to construct a walk based on the corresponding 1D regular mesh of step δ , with p_r , p_c and p_l
 147 the probabilities associated with a computation of the temperatures $T(x + \delta, t - \tau)$ (on the right), $T(x, t - \tau)$ (in the
 148 center) and $T(x - \delta, t - \tau)$ (on the left), respectively. Each move δ requires a time decrement τ . If the temperature at a

149 new location at time $t - \tau$ is unknown, the process is thus continued recursively until a known temperature such as a
 150 boundary (Dirichlet) temperature or the temperature at the initial time is reached.

151 The transition from this kind of walking technique to a three-dimensional grid is straightforward. It was initially
 152 proposed by Haji-Sheikh and Sparrow [31] and allow to simulate a Brownian motion process. However, the previous
 153 example is described so that the purpose of the walk building process can be better understood. This type of walk is
 154 actually not practical when dealing with boundary conditions which are different from Dirichlet in complex geometry
 155 because of the derivative terms with respect to the normal. Therefore the same authors proposed a walk based on a
 156 sphere. In a spherical coordinate system, the formal solution of eq. (1) at a given position \mathbf{x} (here \mathbf{x} is the position in
 157 3D and has thus 3 coordinates) and at time t is:

$$T(\mathbf{x}, t) = \int_{F=0}^1 \int_{G=0}^1 \int_{\tau=0}^t T(\mathbf{x} + \delta\mathbf{u}, t - \tau) dF(\varphi) dG(\theta) dH(\tau) \quad (6)$$

$$\begin{cases} F(\varphi) = \varphi/2\pi, G(\theta) = \frac{1}{2}(1 - \cos(\theta)) \\ H(\tau) = 1 + 2 \sum_{p=1}^{\infty} (-1)^p \exp(-ap^2\pi^2\tau/\delta^2) \end{cases} \quad (7)$$

with δ the radius of a sphere centered in \mathbf{x} , θ the polar angle and φ the azimuthal angle. As in the previous example,
 eq. (6) and eq. (7) also admit a probabilistic interpretation. The quantities F , G and H can be regarded as cumula-
 tive density functions of the azimuthal angle φ , the polar angle θ and the time decrement τ , respectively. The latter
 expression can be thus rewritten:

$$T(\mathbf{x}, t) = \int_{4\pi} p_U(\mathbf{u}) d\mathbf{u} \int_0^{\infty} p_T(\tau) d\tau [\mathcal{H}(t - \tau \leq 0) T_I + \mathcal{H}(t - \tau > 0) T(\mathbf{x} + \delta\mathbf{u}, t - \tau)] \quad (8)$$

159 with $p_U(\mathbf{u})$ and $p_T(\tau)$ the probability densities associated with the sampling of a direction \mathbf{u} and a time τ , respectively.
 160 \mathcal{H} is the Heaviside function. Three random numbers uniformly distributed between 0 and 1 allow us to sample a
 161 direction \mathbf{u} and a time τ . In the case of an infinite medium, the corresponding algorithm to eq. (8) is described in
 162 algorithm 1:

Algorithm 1 Sampling of a conductive path (infinite medium)

Sample a direction of travel \mathbf{u} according to p_U

Sample a time τ according to p_T

if $t \leq \tau$ **then**

$T(\mathbf{x}, t) = T_I$ (initial condition)

else

$T(\mathbf{x}, t) = T(\mathbf{x} + \delta\mathbf{u}, t - \tau)$ (recursivity)

end if

163 Hence, if the initial condition is not reached, the path is placed in $\mathbf{x} + \delta\mathbf{u}$ and the time t associated with the path
 164 is decremented by the quantity τ . A random walk based on the construction of a sphere is generated through iteration
 165 as shown in fig. 1(b). In the case of a finite medium, the conductive path stops if the initial condition or if a boundary
 166 where temperature is known is reached.

167 **2.3. Monte-Carlo Method: radiative path**

168 This paper only deals with the case of an opaque medium and a transparent void phase to simulate experimental
 169 conditions of our previous study [20]. However, the present method is not only limited to this type of interface
 170 condition and can be extended, for example, to the case of a semi-transparent medium or to a convective exchange.

171 In our case, the radiative transfer is thus limited to a surface-to-surface exchange. The coupling between conduction
 172 and radiation is thus carried out at the solid/void interface $\partial\mathcal{D}_{sf}$. The balance of the conductive and the radiative fluxes
 173 is written as follows:

$$\mathbf{n} \cdot \lambda_s \nabla T = \int_{2\pi} |\mathbf{v} \cdot \mathbf{n}| \epsilon (I^0(\mathbf{x}_b) - I(\mathbf{x}_b, -\mathbf{v})) d\mathbf{v} \quad (9)$$

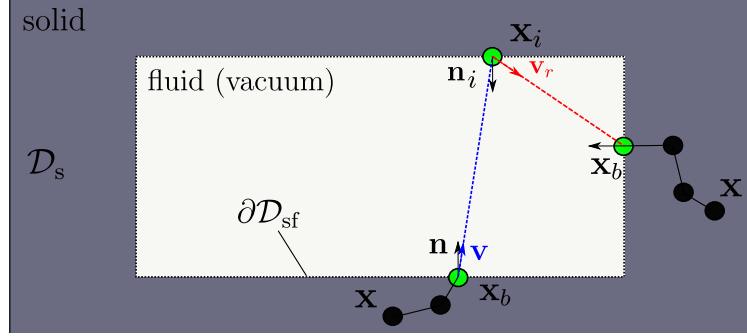


Figure 2: Conductive-radiative coupling, case of opaque surfaces: ray-tracing within the fluid phase (vacuum)

with ϵ the emissivity of the surface (uniform and hemispherical), \mathbf{n} the unitary outward vector normal to the surface, λ_s the thermal conductivity of the solid, \mathbf{x}_b the position at the solid/void boundary, \mathbf{v} the direction, I^0 the blackbody intensity and I the intensity. For the sake of simplicity, radiative quantities averaged on the whole spectrum are considered.

As described in [25], the wall temperature is non-linearly dependent on the blackbody intensity which means the latter must be linearized around a reference temperature T_{ref} :

$$\begin{aligned} I^0(\mathbf{x}_b) &= \frac{\sigma}{\pi} T^4(\mathbf{x}_b) \\ &\approx \frac{\sigma}{\pi} T_{\text{ref}}^4 + 4 \frac{\sigma}{\pi} T_{\text{ref}}^3(\mathbf{x}_b) (T(\mathbf{x}_b) - T_{\text{ref}}) \end{aligned} \quad (10)$$

with σ the Stefan-Boltzmann constant. As previously discussed, this assumption does not pose particular problems in the case of the thermal characterization methods used because of the low temperature elevation of the sample (just a few Kelvin) relative to the equilibrium temperature. As the void phase is transparent, the incident intensity at the wall $I(\mathbf{x}_b, -\mathbf{v})$ is equal to the intensity leaving from \mathbf{x}_i in the direction $-\mathbf{v}$:

$$\begin{aligned} I(\mathbf{x}_b, -\mathbf{v}) &= I(\mathbf{x}_i, -\mathbf{v}) \\ &= \epsilon I^0(\mathbf{x}_i) + \int_{2\pi} p_R(\mathbf{x}_i) \rho' |\mathbf{v}_r \cdot \mathbf{n}_i| I(\mathbf{x}_i, -\mathbf{v}_r) d\mathbf{v}_r \end{aligned} \quad (11)$$

174 with $p_R(\mathbf{x}_i) \rho'$ the Bidirectional Reflectance Distribution Function, which is the product of a probability density over
 175 the reflected directions \mathbf{v}_r and the directional-hemispherical reflectivity. \mathbf{n}_i is the outward normal at the location
 176 \mathbf{x}_i . According to eq. (11), the incident intensity is therefore decomposed into an emission term and a reflection term
 177 integrated over the directions \mathbf{v}_r . In this expression, the incident intensity $I(\mathbf{x}_i, -\mathbf{v}_r)$ can also be decomposed according
 178 to eq. (11), which gives rise to nested integrals and leads to an iterative algorithm. Finally, we can express the incoming
 179 intensity as a function of an intensity emitted from an unknown position \mathbf{x}_γ . The latter intensity can reach the location
 180 \mathbf{x}_b in the direction $-\mathbf{v}$ after zero, one or multiple reflections. For the sake of clarity, the corresponding nested multiple
 181 integrals are simply represented by one integral on the space of optical paths Γ :

$$I(\mathbf{x}_b, -\mathbf{v}) = \int_{\Gamma} p_{\Gamma}(\gamma) I^0(\mathbf{x}_\gamma) d\gamma \quad (12)$$

with $p_{\Gamma}(\gamma)$ the probability density associated with an optical path γ .

By injecting eq. (10) and eq. (12) (linearized) in eq. (9), we can write:

$$\begin{aligned} -\mathbf{n} \cdot \lambda_s \nabla T &= 4\epsilon \sigma T_{\text{ref}}^3 \left(T(\mathbf{x}_b) - \int_{2\pi} \frac{|\mathbf{v} \cdot \mathbf{n}|}{\pi} d\mathbf{v} \int_{\Gamma} p_{\Gamma} d\gamma T(\mathbf{x}_\gamma) \right) \\ &= h_{\text{rad}} \left(T(\mathbf{x}_b) - \int_{2\pi} p_{\mathbf{v}}(\mathbf{v}) d\mathbf{v} \int_{\Gamma} p_{\Gamma} d\gamma T(\mathbf{x}_\gamma) \right) \\ &= h_{\text{rad}} (T(\mathbf{x}_b) - T_{\text{rad}}(\mathbf{x}_b)) \end{aligned} \quad (13)$$

182 with h_{rad} a radiative exchange coefficient. T_{rad} represents an average radiative temperature seen at the interface and due
 183 to the radiative exchanges through the void phase. The latter quantity can be estimated with the following algorithm
 184 (cf. algorithm 2), which is the corresponding algorithmic interpretation of eq. (12) and eq. (13):

Algorithm 2 Sampling of a radiative path: estimate $T_{\text{rad}}(\mathbf{x}_b)$

```

  Sample a direction of travel  $\mathbf{v}$  according to  $p_V$ 
  Evaluate a first intersection  $\mathbf{x}_i$ 
  Sample canonically a random number  $r$  in  $[0, 1]$ 
  if  $r \leq \epsilon$  then
     $T_{\text{rad}}(\mathbf{x}_b) = T(\mathbf{x}_i)$  (absorbed)
  else
    Sample a new direction  $\mathbf{v}_r$  according to  $p_R$ 
     $T_{\text{rad}}(\mathbf{x}_b) = T_{\text{rad}}(\mathbf{x}_i)$  (recursivity)
  end if

```

185 Hence, an emission direction obeying a lambertian law is sampled when evaluating the radiative temperature.
 186 Then, until an absorption event is achieved, the path jumps through the void phase as represented in fig. 2. At each
 187 new reflection, a new direction according to the BRDF is sampled. Each jump does not imply time decrementation
 188 because of the very high velocity of radiative transfers compared to other heat transfer modes such as conduction in
 189 the solid phase.

190 *2.4. Monte-Carlo Method: Computation of the wall temperature*

191 As was the case for the EBE, a finite difference scheme (order 1) requiring the introduction of an infinitesimal
 192 length δ_b is used. The conductive heat flux in eq. (13) is therefore approximated as:

$$-\mathbf{n} \cdot \lambda_s \nabla T \approx -\frac{\lambda_s}{\delta_b} (T(\mathbf{x}_b) - T(\mathbf{x}_b - \delta_b \mathbf{n})) \quad (14)$$

193 By injecting eq. (14) in eq. (13), the wall temperature is expressed:

$$T(\mathbf{x}_b) = \frac{h_{\text{rad}}}{\lambda_s/\delta_b + h_{\text{rad}}} T_{\text{rad}}(\mathbf{x}_b) + \frac{\lambda_s/\delta_b}{\lambda_s/\delta_b + h_{\text{rad}}} T(\mathbf{x}_b - \delta_b \mathbf{n}) \quad (15)$$

Hence, the temperature at the interface in eq. (15) can be interpreted as the average of two temperatures weighed by
 two associated probabilities p_{rad} and p_{cond} :

$$p_{\text{rad}} = \frac{h_{\text{rad}}}{\lambda_s/\delta_b + h_{\text{rad}}} \quad (16a)$$

$$p_{\text{cond}} = \frac{\lambda_s/\delta_b}{\lambda_s/\delta_b + h_{\text{rad}}} \quad (16b)$$

194 The corresponding Monte-Carlo algorithm is straightforward as described in algorithm 3:

Algorithm 3 Computation of the wall temperature $T(\mathbf{x}_b)$

```

  Sample canonically a random number  $r$  in  $[0, 1]$ 
  if  $r \leq P_{\text{cond}}$  then
     $T(\mathbf{x}_b) = T(\mathbf{x}_b - \delta_b \mathbf{n}) = T(\mathbf{x}, t)$  (conductive path cf. algorithm 1)
  else
     $T(\mathbf{x}_b) = T_{\text{rad}}(\mathbf{x}_b)$  (radiative path cf. algorithm 2)
  end if

```

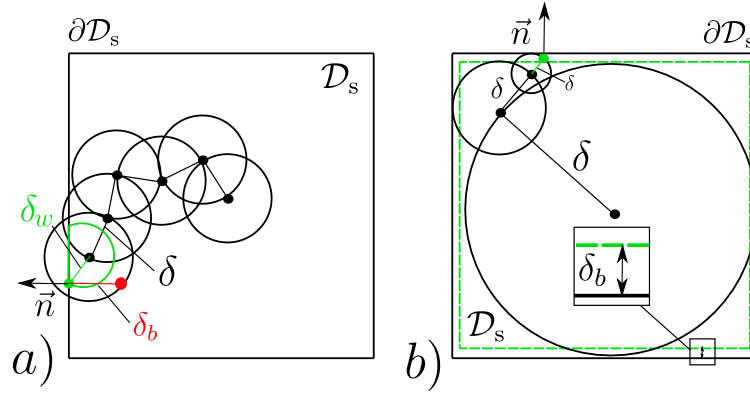


Figure 3: Random walks techniques : a) Fixed random walk b) Floating random walk

2.5. Monte-Carlo Method: Computation of the wall temperature (non diffusive wall)

Considering a given non-emitting ($\epsilon = 0$) wall $\partial\mathcal{D}_\Phi$, excited by a transient heat flux $\Phi(t)$, the balance at the interface is:

$$\mathbf{n} \cdot \lambda_s \nabla T = \Phi(t) \quad (17)$$

As with the finite difference scheme described earlier, the wall temperature can be expressed as:

$$T(\mathbf{x}_b, t) = T(\mathbf{x}_b - \delta_b \mathbf{n}, t) + \Phi(t) \delta_b / \lambda_s \quad (18)$$

This equation can be interpreted with a Monte-Carlo algorithm. If the path reaches an interface with $\mathbf{x}_b \in \partial\mathcal{D}_\Phi$, it is put back at the location $\mathbf{x}_b - \delta_b \mathbf{n}$ and the Monte-Carlo weight is increased by a source term equal to $\Phi(t) \delta_b / \lambda_s$. This kind of procedure is repeated at each contact with the excited surface. In the same manner, if the impacted wall is non-diffusive and adiabatic ($\Phi(t) = 0$), the path is simply put back at the location $\mathbf{x}_b - \delta_b \mathbf{n}$ and the Monte-Carlo weight is not increased.

2.6. Monte-Carlo Method: Random walk techniques

As discussed previously, the generation of the random walk requires the introduction of two arbitrary lengths δ and δ_b which respectively correspond to a displacement within the solid volume and a replacement at the interface. As for the deterministic methods, the computed solution with the MC algorithm converges to the exact solution for $\delta \rightarrow 0$ and $\delta_b \rightarrow 0$. However, as the calculation time increases greatly when the displacement steps are decreased, a compromise is therefore required between the computing cost and precision of the solution.

Moreover, several walking techniques can be employed to mimic the brownian motion [31]. The values of displacement steps δ and δ_b can be alternately fixed or floating. These two different techniques are represented in fig. 3. The first approach consists of setting a fixed value for displacement step δ as shown in fig. 3 a). At each iteration, a direction of travel \mathbf{u} is sampled according to p_U and the distance δ_w between the considered position \mathbf{x} and the boundary $\partial\mathcal{D}_s$ in the direction \mathbf{u} is computed. If $\delta < \delta_w$, the associated boundary condition is processed and the wall temperature $T(\mathbf{x}_b)$ is computed. If the path has to be put back in the solid, a fixed value of δ_b is used. If $\delta > \delta_w$, the path is simply placed in $\mathbf{x} + \delta \mathbf{u}$ with the associated time decrement. Hence, the chosen displacement is computed in the form of $\delta = \min(\delta, \delta_w)$.

As fig. 3 shows, the second technique is based on a floating value of the displacement step δ . The idea is to compute the radius δ_s corresponding to the inner circle. The displacement step is chosen in the form of $\delta = \min(\delta_a, \delta_s)$ with δ_a being an arbitrary value chosen to prevent the displacement being too large. Then, a direction of travel \mathbf{u} is sampled and the jump is performed. If the considered position \mathbf{x} is located between the closest position \mathbf{x}_b to the boundary $\partial\mathcal{D}_s$ and $\mathbf{x}_b - \delta_b \mathbf{n}$, the associated boundary condition is treated. If the path has to be put back in the solid, the same value of δ_b is used and the path is placed in $\mathbf{x} - \delta_b \mathbf{n}$. Finally, each floating displacement δ in the volume also implies a time decrement according to the chosen value of δ .

225 Between these two described walking techniques, the floating random walk was selected and was used to perform our
 226 modeling. Even though the calculation of the inner sphere can be more time-consuming than a fixed walk, it means
 227 we can avoid the introduction of a bias due to a truncated sphere (represented in green in fig. 3 a)). The fixed walk is
 228 also suitable for small values of δ and δ_b .

229 2.7. Monte-Carlo Method: Complete formulation of the algorithm to the calculation of the flash thermogram

230 All the different elements required to solve the considered problem and the construction of the coupled walk in
 231 conduction and radiation were described previously. This section is dedicated to the description of the general archi-
 232 tecture of the algorithm as implemented. Details are given of certain specific elements to make these easier to under-
 233 stand. The aimed configuration to solve is represented in fig. 4. The solid volume \mathcal{D}_s is delimited by the surface $\partial\mathcal{D}_s$,
 234 which is broken down by the surfaces $\partial\mathcal{D}_{fs}$, $\partial\mathcal{D}_{rf}$, $\partial\mathcal{D}_\Phi$ and $\partial\mathcal{D}_p$ respectively corresponding to the fluid(void)/solid
 235 surfaces (diffusive walls), the rear face surface, the excited surface and the adiabatic surfaces (periodicity condition).
 236 Periodicity is also applied in the void phase. Hence, each path reaching this virtual wall (represented in blue) is simply
 237 specularly reflected.
 238

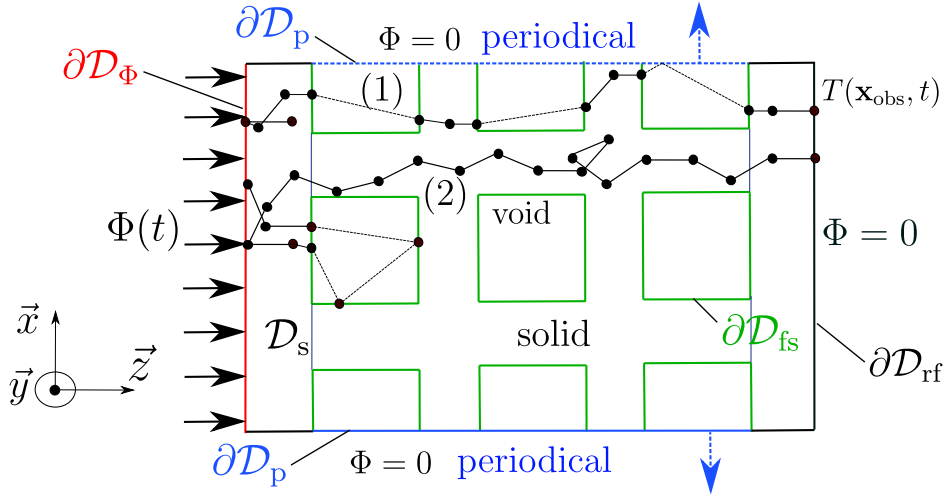


Figure 4: Detailed description of the computation of one realization of the transient conductive-radiative MC algorithm : application to the flash thermogram

239 2.7.1. Initialization

240 We aim to compute the transient mean surface temperature $T_{rf}(t)$ of the rear face, which is defined by:

$$T_{rf}(t) = \frac{1}{S} \int_S T(\mathbf{x}_{obs}, t) dS \quad \forall \mathbf{x}_{obs} \in \partial\mathcal{D}_{rf} \quad (19)$$

with S the surface of the rear face. The latter expression is rewritten to allow a probabilistic interpretation:

$$\begin{aligned} T_{rf}(t) &= \frac{1}{l_x l_y} \int_{x=0}^{l_x} \int_{y=0}^{l_y} T(\mathbf{x}_{obs}, t) dx dy \\ &= \int_{x=0}^{l_x} p_X(x) dx \int_{y=0}^{l_y} p_Y(y) dy T(\mathbf{x}_{obs}, t) \end{aligned} \quad (20)$$

241 with $l_x, l_y, p_X(x) = 1/l_x$ and $p_Y(y) = 1/l_y$ respectively the two lengths of the defined rectangular surface and the two
 242 corresponding probability densities. The initialization can then be easily performed following algorithm 4:

Algorithm 4 Sampling of a spatially averaged temperature: Initialization

Sample location x according to $p_X(x)$
 Sample location y according to $p_Y(y)$
 Set position \mathbf{x}_{obs}
 $T_{\text{rf}}(t) = T(\mathbf{x}_{\text{obs}}, t)$ (recursivity)

 243 **2.7.2. Computation of the Monte-Carlo weight**

All paths start at the time of interest t and at the position \mathbf{x}_{obs} sampled uniformly on the rear face (cf. section 2.7.1). Let us define γ , a given path that reaches the location $\mathbf{x}_\gamma^{(j)} \in \partial\mathcal{D}_\Phi$ (excited surface) for the j^{th} times. This path γ , after a given number of jumps, has an associated time $t - \tau_\gamma^{(j)}$ and the probability density associated with sampling such a path is $p_\Gamma^{(j)}(\mathbf{x}_{\text{obs}})$. Hence, in the space of the paths D_Γ , the rear face temperature calculation can be summarized as:

$$\begin{aligned}
 T_{\text{rf}}(t) &= \mathcal{H}(t - \tau_\gamma^{(1)} \leq 0) \times T_1 + \mathcal{H}(t - \tau_\gamma^{(1)} > 0) \\
 &\times \int_{D_\Gamma^{(1)}} p_\Gamma^{(1)}(\mathbf{x}_\gamma^{(1)}) d\mathbf{x}_\gamma^{(1)} \left[T(\mathbf{x}_\gamma^{(1)} - \delta_b \mathbf{n}, t - \tau_\gamma^{(1)}) + \frac{\Phi(t - \tau_\gamma^{(1)}) \delta_b}{\lambda_s} \right]
 \end{aligned} \tag{21}$$

244 The present algorithm developed for describing the flash method has two important characteristics.

- 245 • A path stops only when the initial condition T_1 (the only known temperature) is reached.
- 246 • As described in section 2.5, the Monte-Carlo weight is incremented when the path reaches the excited face.
- 247 After this kind of interaction, the walk continues as a conductive walk within the solid phase.

 248 Hence, the Monte-Carlo weight associated with the i^{th} realization of the algorithm can be simply written as:

$$\theta_i = T_1 + \sum_{j=1}^{J_i} \underbrace{\mathcal{H}(t - \tau_\gamma^{(j)} > 0) \frac{\Phi(t - \tau_\gamma^{(j)}) \delta_b}{\lambda_s}}_{S_{ij}} \tag{22}$$

with J_i the number of interactions with the excited face of the i^{th} realization of the MC algorithm. Thus, the MC estimator $\bar{T}_{\text{rf}}(t)$ at a given time t is:

$$\begin{aligned}
 \bar{T}_{\text{rf}}(t) &\approx \frac{1}{N_{\text{mc}}} \sum_{i=1}^{N_{\text{mc}}} \theta_i \\
 &= \frac{1}{N_{\text{mc}}} \sum_{i=1}^{N_{\text{mc}}} \left(T_1 + \sum_{j=1}^{J_i} S_{ij} \right) \\
 &= T_1 + \frac{1}{N_{\text{mc}}} \sum_{i=1}^{N_{\text{mc}}} S_i
 \end{aligned} \tag{23}$$

with:

$$S_i = \sum_{j=1}^{J_i} S_{ij} \tag{24}$$

 249 the source term for the i^{th} realization of the MC algorithm. In other words, the temperature of the rear face at a time t
 250 is simply the temperature at the initial condition ($t = 0$) increased by a given amount due to the energy the flash brings
 251 to the front face.

 252 It should be noted that the computation is performed for a given and a unique value of t . Computing an entire
 253 thermogram thus requires time discretization in N_t values in the $[0, t_{\text{max}}]$ interval and the calculation of the temperature

254 performed for each of these times. Efficient and correct storage of the information generated thus far would mean
 255 computing the entire thermogram using only the largest time t_{\max} could be carried out with great rapidity but the
 256 results obtained for different times but computed from the same paths would not be statistically independent. Hence, a
 257 Monte-Carlo calculation composed of N_{mc} paths for each value of the time interval is preferable and thus was carried
 258 out in this work.

259 2.7.3. Complete formulation of the algorithm

260 The complete formulation of the algorithm for one realization of the algorithm is fully described in fig. 5. It
 261 summarizes all the previous described steps of the procedure. The interactions with walls (identified by a surface
 262 mesh) are added and ensure the transition between conductive and radiative paths.

- 263 • The starting point is to sample the starting position on the rear face and to set the starting time (Input, cf.
 264 section 2.7.1). Then, the Monte-Carlo weight and estimator of the source are set at 0.
- 265 • The loop starts with a test which consists in determining if the considered position is on a boundary (TB). If this
 266 test is negative, the conductive path is performed (C1-C5, cf. section 2.2). Otherwise, the algorithm determines
 267 which boundary is reached (TB1 and TB2). If the path is located on the excited face, the estimator of the source
 268 S is increased (B1 and B2, cf. section 2.5).
- 269 • If the path is located on a diffusive wall, a Bernoulli test is performed (B4-B5) to determine whether the path
 270 follows a conductive path in the solid or a radiative path through the void phase (cf. section 2.4).
- 271 • If the path follows a conductive path, it is simply put back (B3) within the solid phase at a distance δ_b from the
 272 boundary. Otherwise, the walk continues as a radiative path (R1-R5, cf. section 2.3)
- 273 • The path is stopped when the associated time becomes negative (cf. section 2.7.2). The resulting Monte-Carlo
 274 weight is stored for this realization of the algorithm and a new path is initialized.

275 3. Validation on combined conductive and radiative transfers: 3D heterogeneous geometry, benchmark con- 276 figuration

277 The purpose of this section is to validate the methodology described above as a direct model for its application in
 278 the framework of an inversion procedure to identify equivalent thermophysical properties. The interest of the method
 279 is highlighted, a step by step development of the coupled thermal problems to be treated is described and benchmark
 280 results are proposed. Firstly, in the case of a flash method configuration, a purely conductive medium is considered.
 281 Then, both conductive and radiative transfers are solved on a one-dimensional problem and an effective thermal
 282 diffusivity is identified. For the sake of brevity, both validation cases are provided in section 7 of the appendices.
 283 Finally, a verification of the solution by comparing with a commercial software like Comsol® is provided on a 3D
 284 heterogeneous geometry.

To validate the MC algorithm to compute the transient solution in the case of a 3D complex geometry, solutions
 obtained by the MC method are compared with more common approaches like the deterministic methods used in com-
 mercial resolution software. As represented in fig. 6(a), a heterogeneous 3D honeycomb geometry was considered.
 This geometry was chosen to be simple enough to be easily reproduced and used as a benchmark for further studies,
 but also complex enough to be comparable to a porous structure made of solid struts which is commonly studied in
 engineering science. It is demonstrated in both section 7.1 and section 7.2 that taking a transient heat flux or periodic
 boundary conditions into account does not cause any particular difficulties. This kind of study can be easily repro-
 duced in future works on the development of the Monte-Carlo method for combined transfers.

The thermal problem is represented in fig. 6(b). z_{\max} and $x_{\max} = y_{\max}$ are the dimensions of the structure. Square
 channels with side $2 \times D_s$ define the void phase while square channels with side D_s represent the struts (solid phase).
 The solid is assumed to be opaque with a unit emissivity. As described in section 2, conduction only occurs in the
 solid phase while radiative transfer only occurs in the void phase.

As represented in fig. 6(b), the thermal boundary conditions are T_{hot} , the temperature imposed on the upper bound-
 ary, T_{cold} , the temperature imposed on the lower boundary and T_{∞} the ambient radiative temperature (infinitely,

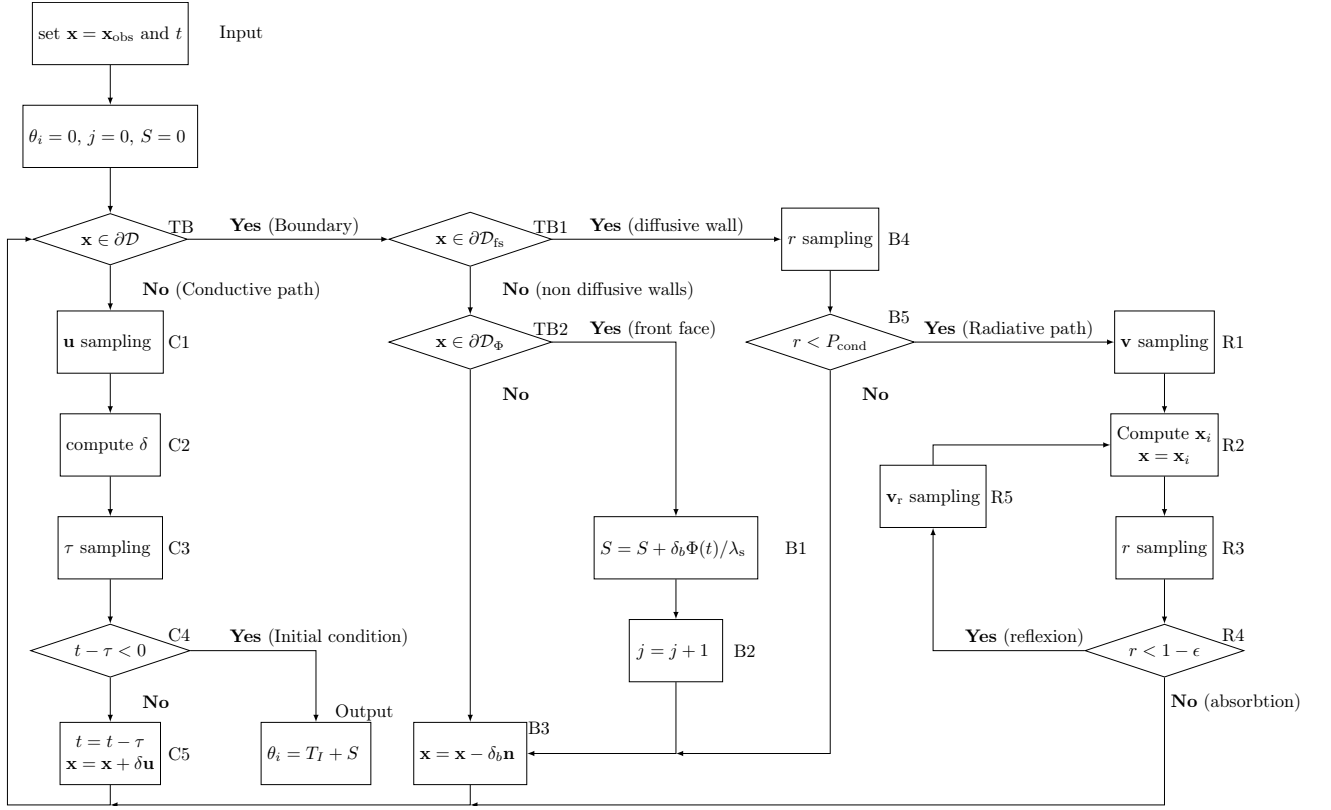


Figure 5: Detailed description of the computation of one realization of the transient conductive-radiative MC algorithm : application to the flash thermogram

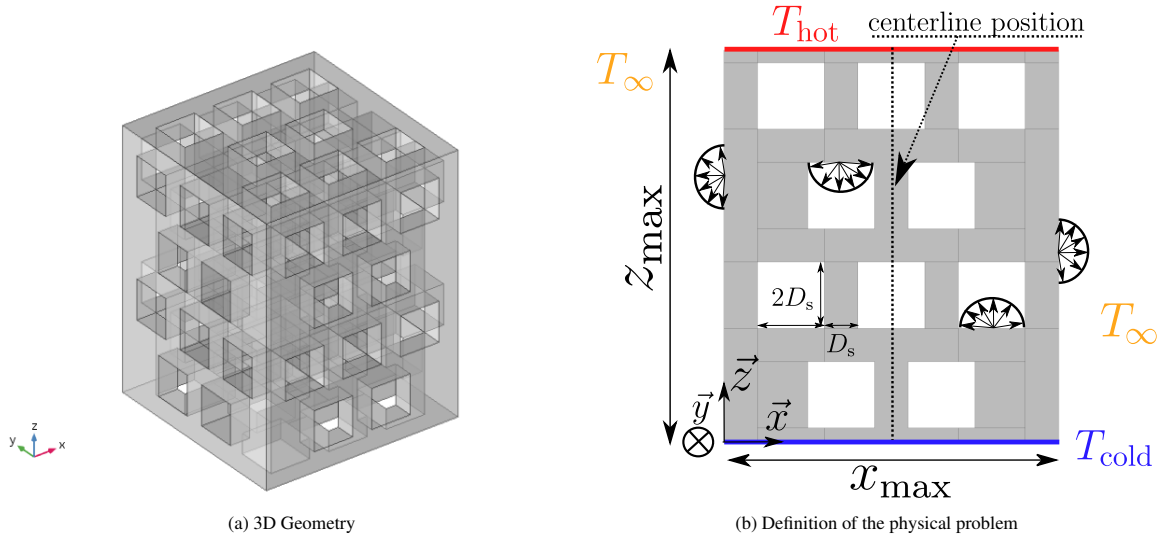


Figure 6: Studied benchmark case

far from the geometry). The structure is under vacuum so that no natural convection can occur. Surfaces can ex-

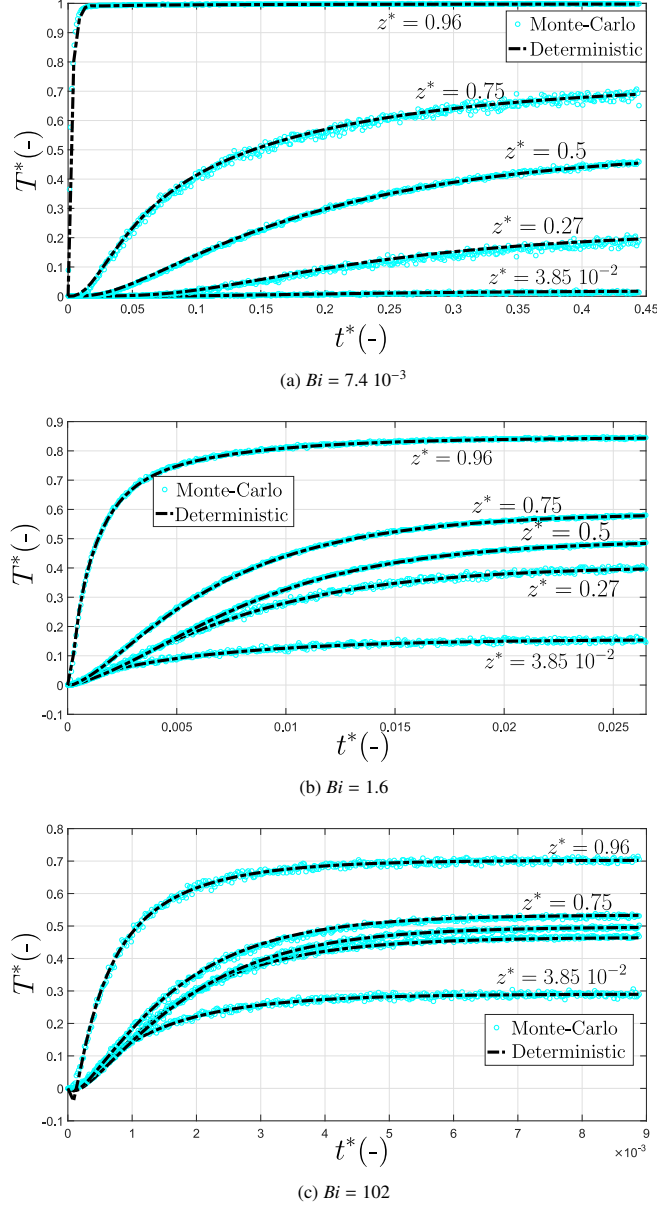


Figure 7: Transient temperature along the z centerline for different values of Biot number and for low temperature gradient $\Delta T^* = 0.1$

change with the environment through radiation. The reference temperature and the ambient temperature are set so that $T_{\text{ref}} = T_{\infty} = (T_{\text{hot}} + T_{\text{cold}})/2$, the average between the two imposed temperatures. At the initial time, the entire structure is in equilibrium at T_{cold} .

Dimensionless temperature differences, radiative Biot number and dimensionless temperature are defined as:

$$\Delta T^* = \frac{T_{\text{hot}} - T_{\text{cold}}}{T_{\text{ref}}}; \quad Bi = \frac{h_{\text{rad}} z_{\text{max}}}{\lambda_s}$$

$$T^* = \frac{T(x_{\text{obs}}, t) - T_{\text{cold}}}{T_{\text{hot}} - T_{\text{cold}}} \quad (25)$$

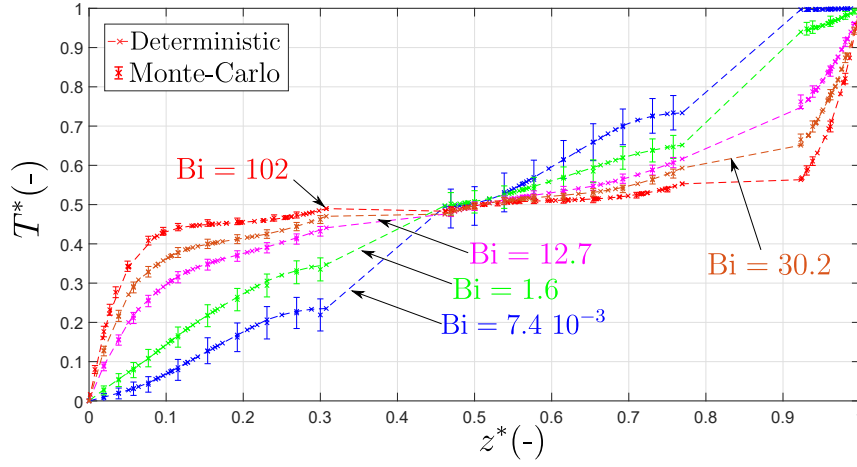


Figure 8: Dimensionless temperature as a function of the dimensionless position for different radiative Biot numbers at steady-state

285 The dimensionless lengths and time are defined such as $z^* = z/z_{\max}$, $y^* = y/y_{\max}$, $x^* = x/x_{\max}$ and $t^* = (\alpha_s t)/z_{\max}^2$.
 286 This problem was solved both by the present Monte Carlo method and by COMSOL multiphysics®. In the case of the
 287 latter, conduction is solved by a finite element method and radiation by the radiosity method, which is well suited to
 288 this problem involving surface-to-surface radiative exchanges. Comsol simulation was carried out using 1900 mesh
 289 points forming 4563 tetrahedrons and 4008 triangles and automatic time step was used
 290 In the case of the Monte-Carlo method, the associated algorithm to solve such a configuration is easily deduced from
 291 the methodology described in section 2. All paths started at the time and position of interest and then a combined
 292 conductive and radiative random walk was performed. A path stopped when a known temperature such as T_{cold} , T_{hot}
 293 or T_{∞} was reached and this temperature was retained as a realization of the MC algorithm. Then, a new path was
 294 initialized. A low dimensionless temperature gradient was deliberately chosen ($\Delta T^* = 0.1$) to ensure the assumption
 295 of linearity of the radiative heat exchanges to be valid.
 296 Transient results obtained with the stochastic and deterministic methods for different positions $z^* = [0.039, 0.27, 0.5, 0.75, 0.96]$
 297 for $x^* = y^* = 0.5$ (centerline position cf. fig. 6(b)) are drawn in fig. 7. Each sub-figure corresponds to:

- 298 • Figure 7(a), $Bi = 7.4 \cdot 10^{-3}$ conduction is dominant
- 299 • Figure 7(b), $Bi = 1.6$ conduction and radiation have a similar influence
- 300 • Figure 7(c), $Bi = 102$ radiation is dominant

301 The dimensionless temperature as a function of the dimensionless time is represented for each radiative Biot number
 302 and position in Figure 8. This figure shows a comparison between the Monte-Carlo method and the deterministic
 303 method at the steady state. The dimensionless temperature as a function of the dimensionless position along the
 304 centerline is drawn.

305 In all cases, a good level of agreement between the two methods is observed, which validates the use of the stochastic
 306 method described to provide a precise solution for a 3D complex geometry and for the thermal problem targeted. The
 307 transient variation of the temperature (thermogram) is correctly calculated with the MC algorithm. We observe an
 308 increase in the rate of heat transfer (it should be noted that the scale of time axis is significantly different for each sub-
 309 graph) with the increase in radiation transfer, i.e. an increase in the total equivalent diffusivity. Moreover, a decrease
 310 in the temperature gradients in the volume due to the increase of radiative exchanges is also noticed. These results are
 311 consistent with the literature on radiative transfer in semi-transparent media.

312 Figure 9 shows one of the main interests of the Monte-Carlo method in our present case. In section 2 we showed
 313 that the geometric complexity can be easily handled with tools provided by the computer graphics community (com-
 314 putation of the intersection between a path and the surface mesh) while the complexity of the problem can be easily

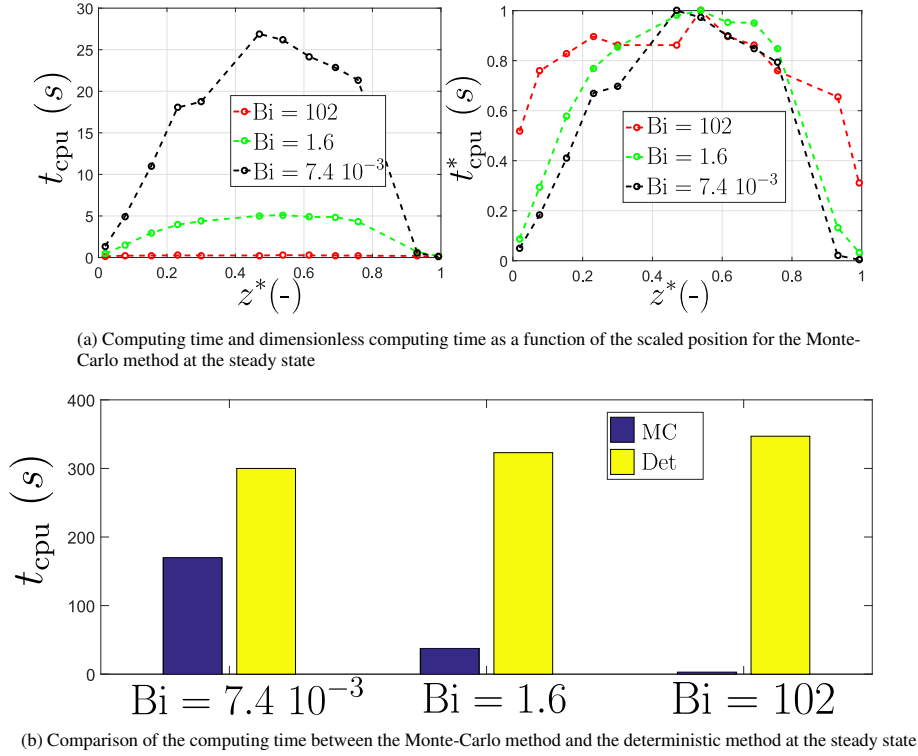


Figure 9: Computing time

315 managed thanks to the formulation of this kind of algorithm (multiple heat transfer modes with a single path). Here,
 316 a reduction of the computational time is observed when the role played by radiation increases. For simple problems,
 317 the effort to perform a MC simulation is more important than a deterministic one. Nevertheless, MC becomes advan-
 318 tageous with the increase of radiative propagation through the void phase.

319 This can be explained at the scale of one path. The calculation time is only linked to the capacity of a given path
 320 to reach a known temperature or heat sources and thus to end the random walk. Hence, it is linked to the speed
 321 of propagation for a given time t of the heat transfer between the source and the position of interest (probe compu-
 322 tation). Assuming there is pure conduction, a path can only walk through the solid following a Brownian motion
 323 until it reaches T_{hot} or T_{cold} . This could be quite tricky, especially with thin struts, and could require a great deal of
 324 computation time. In the case of coupled conductive and radiative heat transfer, the paths can follow a radiative path
 325 through the void phase, which allows them to travel along a straight line between two interfaces. The distance traveled
 326 in one step of the algorithm is very large, especially through large void channels, compared to the distance traveled
 327 during one step of the conductive random walks. Hence, a path can reach T_{hot} , T_{cold} or even T_{∞} in a smaller number
 328 of iterations of the MC algorithm. Moreover, this kind of phenomenon increases with the increase of the probability
 329 to follow a radiative path.

330 Figure 9 represents the computing time and the dimensionless computing time according to the position z^* to perform
 331 a given number of realizations of the Monte-Carlo algorithm and for three different radiative Biot numbers on a single
 332 CPU Intel Xeon X5650. We note that:

- 333 • The computation time for a position at the center $z^* = 0.5$ logically corresponds to a maximum. This position
 334 is indeed the furthest from the known temperatures.
- 335 • The computation times decrease when the radiative transfer increases. This can be explained by the increase of
 336 the number of sampled radiative paths as described previously.

- The dimensionless computation times become insensitive to the starting position with the increase of radiative transfers. This can also be explained by the increase of the number of sampled radiative paths. Paths would evolve preferentially in the void phase and reach a known temperature with a low number of steps, whatever the starting point.

Figure 9(b) shows the computing time required to compute the temperature for all the 11 positions for the same radiative Biot numbers in fig. 9(a) with the MC algorithm. It is compared to the computing time required with the deterministic method (Comsol ®) to obtain the whole field of temperature. The number of realizations of the MC algorithm was deliberately set to obtain a similar computing time between both methods for $Bi = 7.4 \times 10^{-3}$. As we have explained, it can be noted that the computing time needed with the MC method strongly decreases with the increase of the radiative transfers thus demonstrating better performances in this case. The access of the whole temperature field is not limiting as long as only a probe computation is required in the case of a characterization procedure. This study thus provides advice on choosing a method for a possible user. The deterministic method is preferable for high porosity media and purely conductive transfer while the Monte-Carlo method described was found to give better performances with coupled transfers.

4. Application to the characterization of porous media

The purpose of this section is to apply the proposed procedure to a numerical thermophysical characterization of heterogeneous structures. Firstly, the construction of the 3D surface mesh and the inversion procedure are detailed. Then, a parametric investigation of the different data of the problem is performed on Kelvin cells, which are commonly used as the geometry of reference in the frame of foams.

4.1. Studied geometries and construction

3D foam geometries are constructed using 3D images defined by structured grids of $V_x \times V_y \times V_z$ voxels, which can be obtained numerically (with a specific software) or experimentally with a scanning method like X-ray tomography. This article deals with the case of purely numerically generated foams with a structured matrix. They are based on a repetition of a unitary tetrakaidecahedron (Kelvin cell) or of a cubic-shaped cell as used in the validation section (cf. section 3). Nevertheless, as highlighted, the proposed method is easily expandable to a wide range of geometries such as randomly distributed matrix foams, fibers, packed spheres or even real x-ray tomographed foams. The initial raw data were obtained from a foam generator software named GenMat ®, which was developed by LTEN (Heat Transfer and Energy Laboratory at Nantes - UMR CNRS 6607) and IUSTI (Institut Universitaire des Systèmes Thermiques et Industriels - UMR CNRS 7343). Based on a watershed marker-based method, foams numerically generated by this software were validated by comparing with a reference SiC foam [10].

GenMat ® provides a stack of grayscale images corresponding to the desired foams. Two stacks of plain material corresponding to the two soleplates (cf. section 1) were added. Then, the surface mesh was generated with a robust marching-cube method available in 3DSlicer ® (open-source software). Smoothing algorithms (surface preserved) or decimation algorithms (reducing the mesh refinement) can be also used and are available in Meshlab ® and Blender ® (open-source softwares). Finally, a good quality closed mesh was obtained as shown in fig. 10.

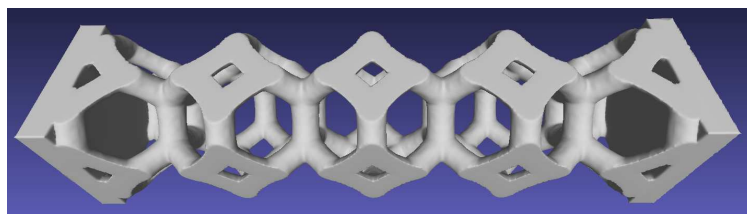


Figure 10: Example of the studied geometry: four Kelvin cell sandwiched between two soleplates

372 4.2. Inversion of the thermogram - equivalent properties of the medium

373 The transient evolution of the temperature on the rear face is treated exactly as if it were an experimental thermo-
374 gram. As the thermogram was obtained using a stochastic approach, the temperature calculated at any time is affected
375 by a random error. It should also be noted that the standard deviation associated to each point is easy to obtain, which
376 is one of the strengths of the Monte Carlo methods [32]. This standard deviation is proportional to the inverse of the
377 square root of the number of Monte Carlo realizations (or of the computation time, this one being proportional to the
378 number of calculated random walks in the medium). From the inversion point of view, this error is similar to the noise
379 observed in an experimental thermogram obtained with a flash method (cf. section 7.1).

380 The inversion of the thermogram requires a direct model of the equivalent homogeneous media like any kind of in-
381 verse problem. Here the direct model aims to calculate the thermogram at the rear face of a homogeneous sample
382 sandwiched between two soleplates. This thermogram is indeed the quantity provided by the Monte-Carlo algo-
383 rithm. The thickness and thermal properties of the two soleplates are known and correspond to the values used in the
384 Monte-Carlo code. The homogeneous medium representing the foam is characterized by its total equivalent thermal
385 conductivity and equivalent specific heat. The direct model used for the inversion procedure is a 1D three-layer purely
386 conductive model. The thermal problem is solved with a quadrupole method [33], which provides a simple semi-
387 analytical solution. The equivalent total thermal diffusivity of the foam can be identified using this inverse method.
388 The total equivalent conductivity can be deduced from the knowledge of the specific heat of the foam and its porosity.
389 A Levenberg-Marquardt algorithm [34] was used to obtain the best match between the thermogram calculated on the
390 actual sample structure (foam struts) with the Monte Carlo algorithm presented above and the thermogram calculated
391 with the equivalent homogeneous medium. More details about inversion procedure can be found in the authors' paper
392 devoted to characterization of foams at high temperature by using the Flash method [20].

393 4.3. Parametric study and discussions

394 4.3.1. Influence of the reference temperature

395 The algorithm described in section 2 and validated herein above was applied to a porous medium composed of a
396 stack of five Kelvin cells between two soleplates as depicted in fig. 10. Periodic boundary conditions were applied
397 along the x and y directions such that an infinite medium was actually considered along these two directions (cf. fig. 4).
398

399 The conductivity of the solid phase was fixed at $\lambda_s = 50 \text{ W} \cdot \text{m}^{-1} \cdot \text{K}^{-1}$ (which is close to the thermal conductivity
400 of SiC at 1000 K), the diameter of the cell was $D_{\text{cell}} = 10 \text{ mm}$, the porosity of the foam was $\varepsilon = 80 \%$, the investi-
401 gated range of the reference temperature was between 300 K and 2500 K. The specific heat of the solid was set at
402 $10^6 \text{ J} \cdot \text{m}^{-3} \cdot \text{K}^{-1}$ and the duration of the heat flux flash was set so that $t_d = t_{\text{max}}/50$ (cf. eq. (27)). Let us note that
403 taking constant thermal properties of the strut material along the whole temperature range from ambient to 2500 K is
404 nonphysical. However, the goal of this study was not to describe the variation of the total equivalent conductivity of a
405 real foam but to conduct a parametric study aiming at separating the influence of the different parameters (temperature,
406 porosity, cell size, bulk conductivity and emissivity), that involves rightly to keep all parameters constant except the
407 parameter of interest. Such study is easily feasible numerically whereas it is difficult to be carried out experimentally
408 due to sample availability or due to correlations between parameters and reference temperature.

409 Figure 11 shows the different numerical thermograms obtained with the MC algorithm and corresponding best fits
410 after the estimation procedure based on the three-layer purely conductive and homogeneous model. A good level of
411 agreement is observed. This figure shows clearly the acceleration of the thermograms when the reference temperature
412 increases because of the increasing role of radiation. It should be noted that the temperature reached at the steady
413 state is the same for all reference temperatures because the deposited energy was the same. Each thermogram was
414 computed using 2000 Monte-Carlo realizations per time interval and 50 time intervals (thus 10^5 total random walks
415 were computed in total).

416 The right part and left parts of fig. 11 show an example of random walk in the structure at a low reference temper-
417 ature (for which heat transfer is almost purely conductive) and at a high reference temperature ($T_{\text{ref}} = 2500 \text{ K}$) (for
418 which radiation plays a significant role), respectively. As previously stated, when the reference temperature increases,
419 the probability of following a radiative path increases. Thus an increasing number of paths (blue lines in insets in
420 fig. 11) cross the void phase. This travel is quasi instantaneous (due to the high velocity of light), so the mean celerity
421 (*i.e.* the total equivalent thermal diffusivity) of the heat transfer increases. Hence, the increasing role played by the

422 radiative transfer means the steady state is reached more quickly. This means the starting time of the paths can be
 423 decreased which causes a strong decrease in computation time as explained in section 3. With a single CPU Intel Xeon
 424 X5650, a gain of a factor of 50 is observed between a pure conduction calculation and a calculation performed with
 425 $T_{\text{ref}} = 2500$ K. Hence, the MC algorithm is of interest when radiative heat transfer plays an important role, as was
 426 already explained in the previous section. An opposite trend is generally observed following deterministic methods
 427 for conduction-radiation algorithms which slow down when the radiation contribution increases due to error control.
 428 For each reference temperature value, fitting the computed thermogram makes it possible to obtain a total equivalent
 429 diffusivity of the porous medium. In the following subsections, the influence of the foam's morphological (number
 430 of cells, porosity, cell size) and thermophysical (bulk thermal conductivity, emissivity) properties on the equivalent
 431 diffusivity are presented. For the sake of brevity, the thermograms will no longer be shown.

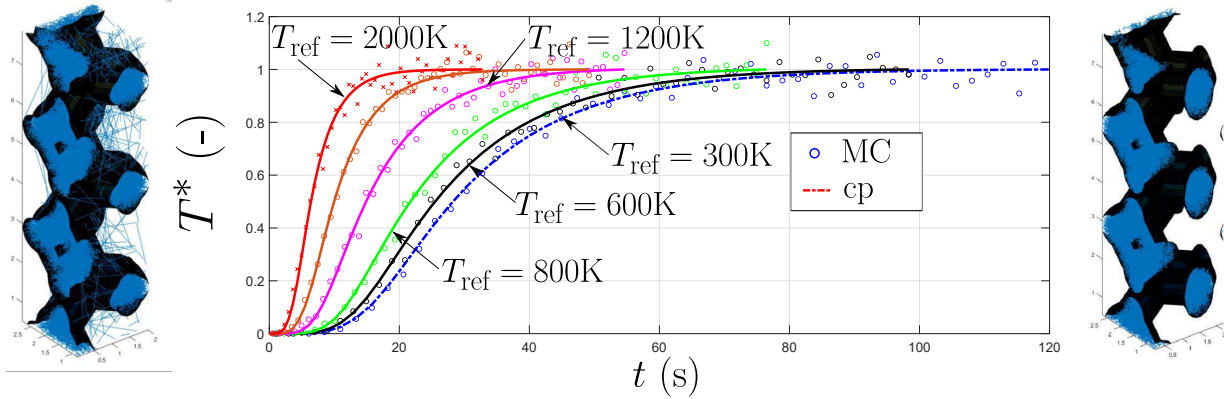


Figure 11: Numerical thermograms (symbols) and corresponding thermogram fits (plain lines) obtained with the three-layer purely conductive and homogeneous model (cp). Right and left insets: representation of random walk paths (blue lines) inside the structure. Right inset: 300K temperature, radiation is negligible most of the random walk stays inside the struts. Left inset: 2500 K, the random walk can jump straightly from one strut to another strut

432 4.3.2. Influence of the number of pores in the thickness

433 The variation of the pore number in the thickness allows us to address the question of the validity of the diffusion
 434 approximation to describe the radiative transfer. This assumption is based on the idea that radiative transfer is com-
 435 parable to a diffusive transfer such as conduction. This means the radiative transfer can be described by the simple
 436 definition of a “radiative” conductivity λ_{rad} . In the case of an optically thick participating medium, Rosseland’s law
 437 [35] is commonly used:

$$\lambda_{\text{rad}} = \frac{16\sigma T_{\text{ref}}^3}{3\beta_{\text{eff}}} \quad (26)$$

438 The effect of increasing the number of pores in the thickness is that the equivalent optical thickness of the porous
 439 medium also increases and thus, the diffusion approximation according to Rosseland becomes valid.

440 Five foams were generated which were exactly identical in terms of porosity and pore size. These foams differ simply
 441 by the number of patterns present in the thickness such as represented in fig. 12. The conductivity of the solid was
 442 decreased to $1 \text{ W} \cdot \text{m}^{-1} \cdot \text{K}^{-1}$ to increase the role of the radiative transfer. For these five foams, the total equivalent
 443 estimated conductivity was drawn according to the reference temperature. First, when the reference temperature is
 444 low, the equivalent total conductivity is identical between the different structures. This is due to the fact that in pure
 445 conduction the equivalent conductivity is independent of the number of patterns. A single cell is sufficient to be
 446 representative of the transfers. Secondly, with the increase of the radiative transfer, the total equivalent conductivity
 447 increases with the number of pores.

448 The Rosseland’s law given in eq. (26) predicts that the equivalent “radiative” conductivity, for a given reference
 449 temperature, does not vary with the thickness. Thus, if the medium is optically thick, the transfer by radiation only
 450 depends on the equivalent extinction coefficient and the reference temperature. We can observe graphically that the

451 equivalent total conductivity for a foam with 3 cells and 4 cells are very close to that of a foam with 5 cells. This
 452 suggests, at least graphically, the validity of the diffusion approximation and a radiative behavior in agreement with the
 453 Rosseland prediction for the chosen set of parameters and investigated range of reference temperature. The proposed
 454 tool enables the quantification of an equivalent radiative conductivity, an exploration of the validity of the diffusion
 455 approximation and a simplification in the modeling. In the following, only foams with at least 4 cells along the
 456 thickness are considered.

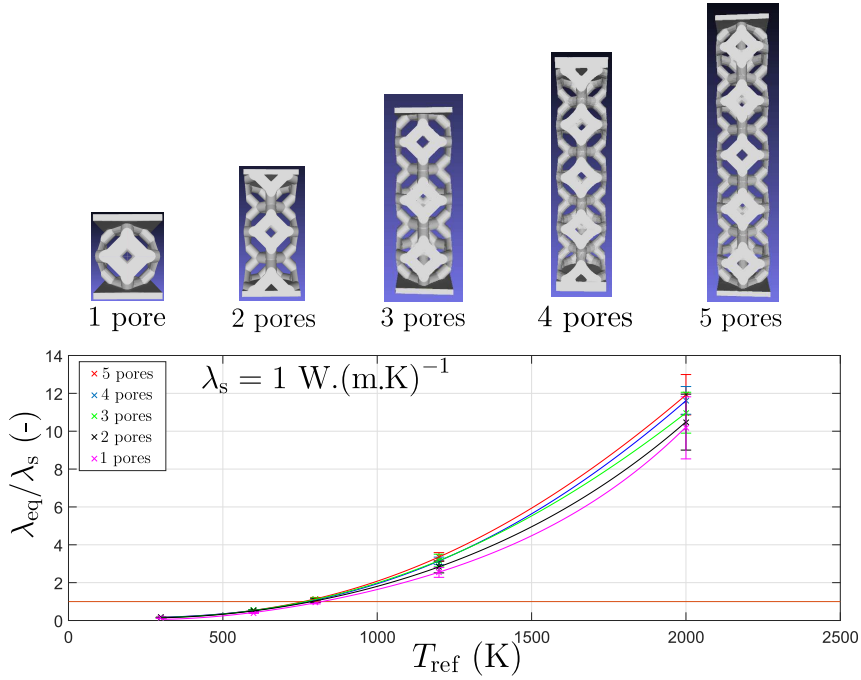


Figure 12: Influence of the number of pores in the thickness – $\lambda_s = 1 \text{ W} \cdot \text{m}^{-1} \cdot \text{K}^{-1}$, $\varepsilon = 80 \%$, $D_{\text{cell}} = 10 \text{ mm}$

4.3.3. The influence of the porosity

457 In this section the influence of the porosity and shape of the solid matrix on the coupled heat transfer is presented.
 458 Two kinds of cell geometries were considered: Kelvin cell and honeycomb cell (cubic-shaped cell) as represented in
 459 fig. 13. Cell size is set to 2 mm. A stack of 4 cells along the heat transfer axis was considered. For each structure,
 460 the porosity value of both structures varied from 0.2 to 0.8. The evolution of the total equivalent conductivity as a
 461 function of the reference temperature is drawn.

462 For a given porosity, a logical linear increase in the total equivalent conductivity with the third power of the refer-
 463 ence temperature is observed (cf. Rosseland relation eq. (26) or according to other laws dedicated to radiative
 464 conductivity [36]). At a low temperature, heat transfer arises from conduction only and a very well-known result
 465 is observed[2], *i.e.* the higher the porosity, the smaller the conductivity. Conversely at high temperature, the higher
 466 the porosity, the higher the conductivity is because the emptier the structure, the easier radiation can take place and
 467 transfer heat. We notice that the conductivity depends little on the porosity at a given temperature near 1200 K ($4\sigma T^3$
 468 $= 400 \text{ W} \cdot \text{m}^{-2} \cdot \text{K}^{-1}$) in this example, except for the lowest porosities. Moreover, the influence of the shape of the
 469 matrix is highlighted. For the same set of parameters, the total effective conductivity of the cubic-shaped cell is greater
 470 than the Kelvin cell. This leads to the idea that a cubic shaped foam is more transparent than a Kelvin cell foam, *i.e.*
 471 it has a lower effective extinction coefficient. The slope of the curve presented in fig. 13 means a radiative coefficient
 472 equivalent to the porous medium could be extracted following a judicious choice of an equivalent radiative law.

473 These results seem logical and expected. The proposed procedure involves retrieving the classic results from the
 474 literature to explore the influence of parameters like porosity and carry out a better quantification of the major heat
 475

476 transfer mechanism for a given structure. In the case of pure conduction, the estimated conductivity is compared to
 477 the one proposed by Pabst *et al.* [37] for a Kelvin cell with the same morphological parameters. As presented in
 478 fig. 14, a good level of agreement is found which meant the result could be validated with a high level of confidence
 479 in the proposed method.

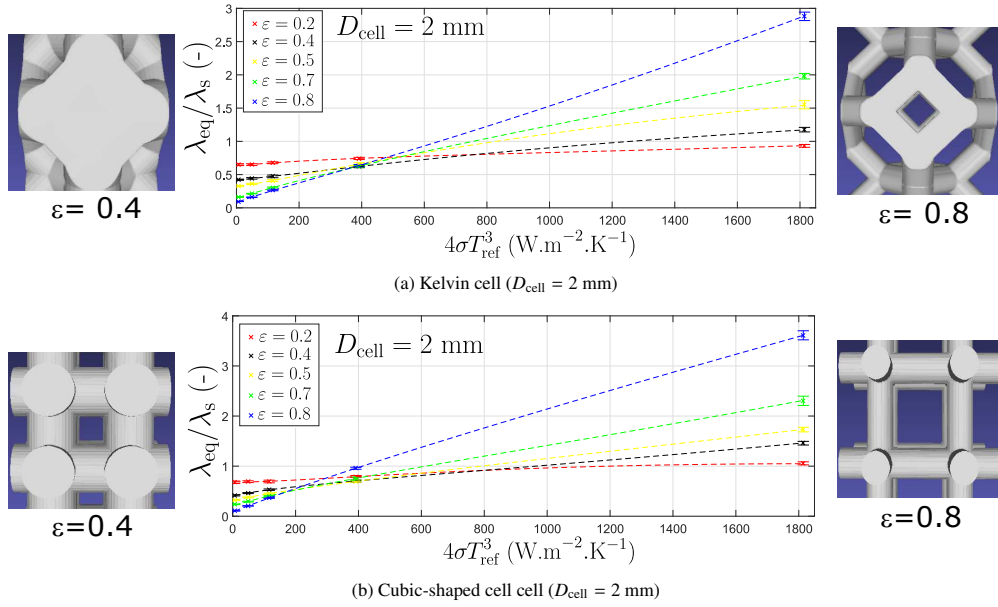


Figure 13: Influence of the porosity on the total heat transfer – $\lambda_s = 1 \text{ W} \cdot \text{m}^{-1} \cdot \text{K}^{-1}$, $D_{\text{cell}} = 2 \text{ mm}$

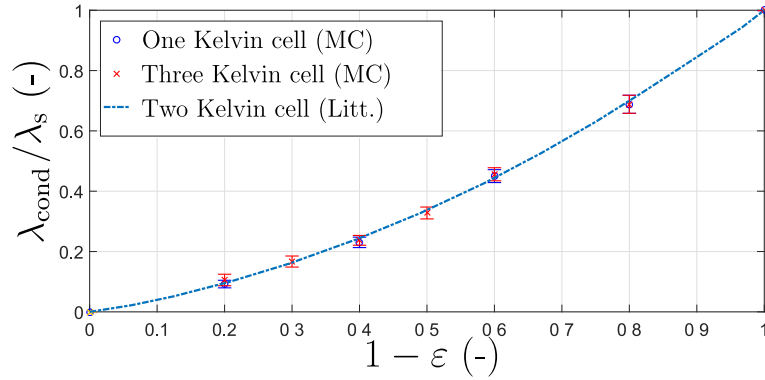


Figure 14: Equivalent thermal conductivity of Kelvin cell according to porosity: pure conduction

480 4.3.4. The influence of cell size

481 This section focuses on the influence of cell size. The geometry studied was composed of four Kelvin cells with
 482 a fixed porosity equal to 80%. We varied the cell size between 1 mm and 10 mm. The equivalent conductivity as a
 483 function of the third power of reference temperature is represented in fig. 15. In pure conduction (low temperature),
 484 the equivalent conductivity does not depend on cell size. The solid matrix is organized in exactly the same way and
 485 the amount of material (porosity) is the same which means there is no reason to observe an influence of cell size.

486 This is a well-known result in foam literature [2]. When the temperature increases, radiation transfers increase too
 487 and we observe that the larger the cell size, the higher the total equivalent conductivity of the homogeneous medium.
 488 As noted in the previous section, this result is logical. The mean free radiative path is indeed greater for larger cells,
 489 which corresponds to a lower extinction coefficient. It should be noted that, in theory, the equivalent optical thickness
 490 is the same for all these different structures. However, as the sample thickness increases when the size of the cell
 491 increases, this corresponds to a decrease in the extinction coefficient β (the optical thickness being defined by $\tau = \beta e$)
 492 and thus an increase in radiative conductivity as predicted, for example, by the Rosseland model.

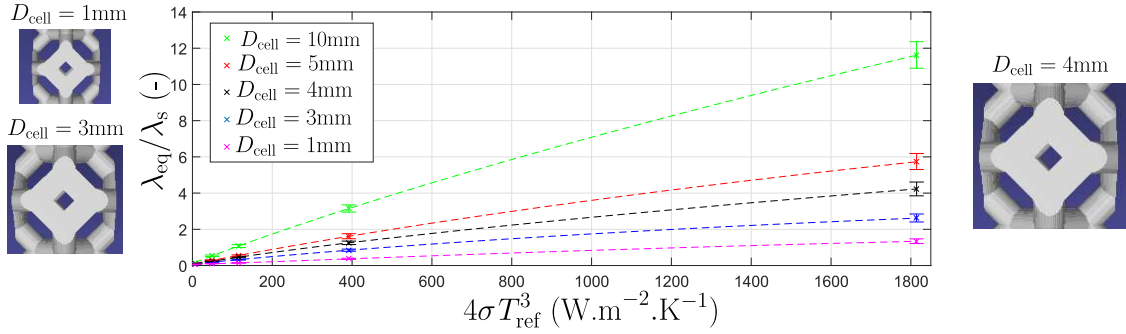


Figure 15: Influence of cell size on the total heat transfer: Kelvin cell – $\lambda_s = 1 \text{ W} \cdot \text{m}^{-1} \cdot \text{K}^{-1}$, $\varepsilon = 80 \%$

493 4.3.5. Influence of the bulk conductivity of struts

494 In fig. 16, the results obtained for a stack of 4 Kelvin cells with a porosity equal to 0.8 and bulk conductivity of
 495 the struts varying from $0.1 \text{ W} \cdot \text{m}^{-1} \cdot \text{K}^{-1}$ to $100 \text{ W} \cdot \text{m}^{-1} \cdot \text{K}^{-1}$ are described. This study illustrates how conduction
 496 and radiation through the porous medium are in a competition to become the major heat transfer mechanism.

497 The ratio $\lambda_{\text{eq}}/\lambda_s$ is presented in fig. 16(a). If the temperature is low enough for heat transfer to be due to conduction
 498 alone, then the equivalent conductivity is proportional to the bulk conductivity and consequently the ratio $\lambda_{\text{eq}}/\lambda_s$
 499 is logically independent of the thermal conductivity of the solid. This ratio only depends on structural properties such
 500 as porosity and the shape of the solid matrix. When the temperature increases, the ratio is no longer independent on
 501 the bulk conductivity because of the increasing role of radiation transfer, which becomes quickly the main transport
 502 mode when the thermal conductivity is low.

503 Figure 16(b) presents the ratio of the radiative thermal conductivity by the total equivalent conductivity (percent-
 504 age) as a function of the reference temperature for different conductivities of the bulk is represented. For a low bulk
 505 conductivity (e.g. $\lambda_s = 0.1 \text{ W} \cdot \text{m}^{-1} \cdot \text{K}^{-1}$), radiation transfer very quickly becomes the main transfer method, even
 506 for low reference temperatures. For example, for $T_{\text{ref}} = 500 \text{ K}$, radiation accounts for already almost 60 % of the
 507 total transfer. On the other hand, for $\lambda_s = 100 \text{ W} \cdot \text{m}^{-1} \cdot \text{K}^{-1}$, conduction transfer remains predominant over radiation
 508 transfer even at high temperatures.

509 These observations can be understood through the scope of the stochastic method developed in this paper. Indeed,
 510 the competition between the two heat transfer modes appears because of the probability of following a radiative
 511 path P_{rad} . If the conduction term λ_s/δ_b is very large compared to the radiative term h_{rad} , then the problem is purely
 512 conductive and it is weakly sensitive to radiative transfer and thus to temperature. On the other hand, considering
 513 an extreme case in which the radiation is very large in comparison to the conduction, the total heat transfer does not
 514 depend on the conductivity of the solid.

515 4.3.6. The influence of emissivity

516 In this section, the influence of the emissivity of struts on the total equivalent heat transfer is studied. In all
 517 previous cases, the emission of radiation was hemispherical (lambertian or isotropic on the hemisphere) and the
 518 emissivity was chosen equal to 1. On a structure composed of a stack of five Kelvin cells along the direction of
 519 heat transfer, simulations were performed for an emissivity and a reference temperature varying between 0 to 1 and

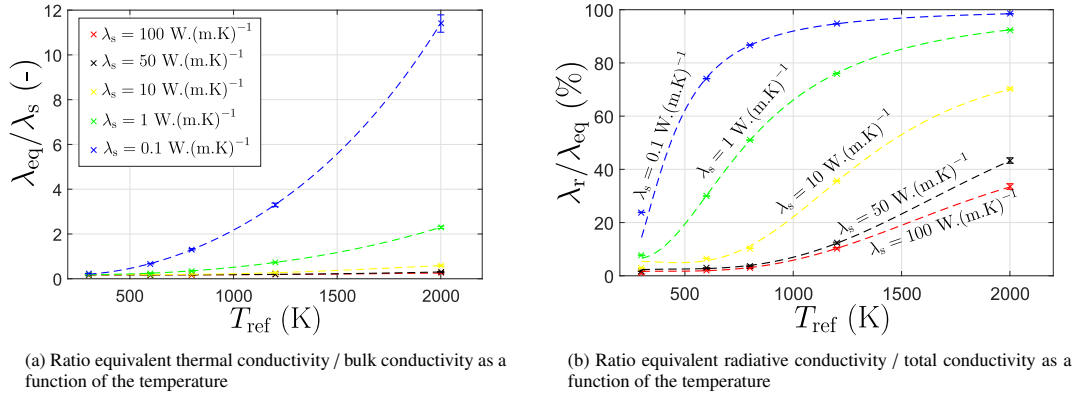


Figure 16: Influence of the bulk conductivity for a structure composed of 4 Kelvin cells – $\varepsilon = 70\%$, $D_{cell} = 2$ mm

520 300 K to 2500 K, respectively. fig. 17 shows the ratio λ_{eq}/λ_s as a function of the reference temperature. In this work,
 521 perfectly diffuse reflection was implemented. Nevertheless, it is possible to take specular reflection or combined
 522 specular/diffuse reflection into account using the proposed stochastic approach.

523 When transfers by radiation are weak, the emissivity logically has no influence on the equivalent total conductivity
 524 because conduction is the main mode of transfer. Then, with the increase of the reference temperature (*i.e.* radiation),
 525 an increase of the equivalent conductivity with the emissivity and, logically, with the temperature considered, is
 526 observed. For the asymptotic case $\varepsilon = 0$, no radiative transfer can occur. Then, a rapid increase in total equivalent
 527 conductivity between $\varepsilon = 0$ and $\varepsilon = 0.25$ is observed and reaches its maximum for $\varepsilon = 1$. In the case of an optically
 528 thick medium, this kind of phenomenon can not be explained by the influence of the emission of the intern part of the
 529 two soleplates alone. An effective optical thickness of the porous medium, which can be seen as the statistical mean
 530 free paths traveled within the fluid phase and thus depends only on the morphological properties of the foam, appears
 531 here to depend on the emissivity. Evidence on this kind of result was also given by Vignoles [15], Patel et al. [21] or
 532 Li and Wang [38]. The latter also showed that the specular/diffuse mode of reflection has a major role on the effective
 533 extinction coefficient. This aspect could usefully be explored in more detail in further studies.

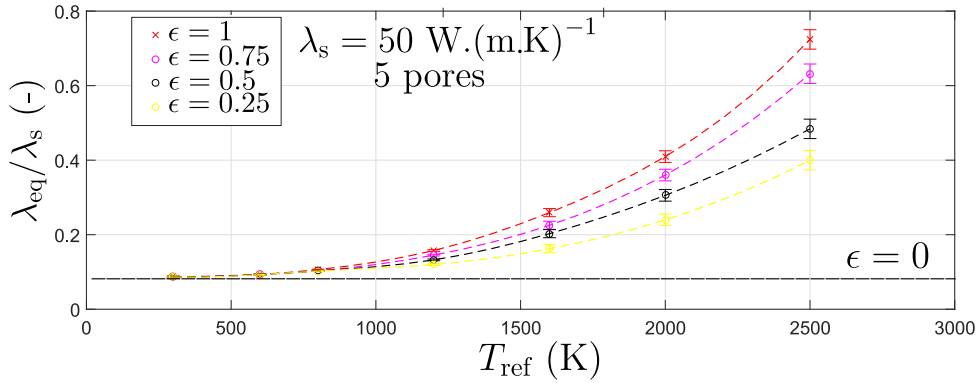


Figure 17: Influence of the emissivity of struts – $\lambda_s = 50$ W · m⁻¹ · K⁻¹, $\varepsilon = 70\%$, $D_{cell} = 2$ mm

534 5. Conclusion

535 In this paper, a new tool for modeling and characterizing coupled transfers in complex geometric media such as
536 porous media was proposed. The recent developments of the Monte-Carlo method make it possible to imagine, in
537 the framework of linear thermal transfers, to solve coupled and multiphysics transfers with a single algorithm. This
538 method is very interesting for the characterization of complex media for two reasons. Firstly its capacity to han-
539 dle the increasing complexity of the solved physics (directional dependency of emission, semi-transparent medium,
540 frequency dependence, anisotropy of the solid phase, etc.) without an increase in computation time. Secondly the
541 calculation performances allowed by using tools from the graphic community (insensitivity of the refinement of the
542 mesh, parallelization, etc.) make it an effective option as well. Moreover, the probe computation aspect, the statistical
543 interpretation of the space of paths and the approach's capacity to simulate the combined heat propagation are very
544 appropriate in the context of study and understanding of coupled mechanisms. For the first time, a numerical repro-
545 duction of the flash method in the case of coupled conductive and radiative transfers (opaque surfaces) was performed.
546 Firstly, the methodology was fully described. This highlighted the proposed formulation's various positive aspects
547 such as its practical implementation and the understanding it provides of the intrinsic thermophysical properties
548 through probabilities. However, the method requires the introduction of arbitrary lengths to generate the walk. Future
549 studies will focus precisely on determining a time/accuracy trade-off for these parameters.

550 Next the proposed MC algorithm and its use as a numerical measuring instrument were validated by comparison with
551 deterministic solvers such as FlexPde®, Comsol® or a semi-analytical solution provided by the quadrupole method.
552 A validation of the transient solution was provided on a 3D heterogeneous benchmark case. The results showed a
553 very good level of agreement with deterministic solvers and highlighted the interest of using the present method in
554 the case of an increasing influence of the radiative transfer. New transport modes such as advection, conduction in the
555 fluid phase and participating solid phase can be added.

556 Finally, this code was used to reproduce the usual flash method applied to experimentally determine the diffusivity of
557 foams, as was recently performed by the authors. The thermal response of a foam sample sandwiched between two
558 soleplates and submitted to a heat radiative flux flash was computed. The thermogram obtained numerically were fitted
559 against the thermogram obtained with a direct model involving a homogeneous medium between the same soleplates.
560 A total equivalent diffusivity (conduction+radiation) for the foam was thus obtained. The proposed procedure and its
561 coupling with recently developed tools such as GenMat® (foam generator) enabled us to propose a parametric study
562 of how morphological and thermophysical parameters influence the equivalent total conductivity of the foam. Our
563 results showed a good level of agreement with the associated literature. The proposed method can be adapted to new
564 geometries and to new characterization configuration. Further studies could focus on new heterogeneous structures
565 such as X-ray tomographed foams, numerical foams, packed sphere or fibers and new characterization methods such
566 as the hot-guarded plate or the hot-wire method used to study combined heat transfer. Hence, correlations of effective
567 equivalent properties of such media could be provided in parallel of experimental developments.

568 6. Acknowledgements

569 The authors gratefully acknowledge Benoit Rousseau (LTEN - UMR CNRS 6607) for providing and support
570 regarding the use of GenMat. We also wish to acknowledge Cyril Caliot (LMAP - UMR CNRS 5142), Mouna El
571 Hafi (RAPSODEE - UMR CNRS 5302), Richard Fournier and Stephane Blanco (LAPLACE - UMR CNRS 5213) for
572 their motivating advice and the fruitful discussions. We would like to thank the Meso-Star start-up and the EDStar
573 platform for making their libraries *Star-Engine* available to us and for the support provided. High Performance
574 Computing resources were partially provided by the EXPLOR centre hosted by the Université de Lorraine

575 References

- 576 [1] A. Sommers, Q. Wang, X. Han, C. T'Joen, Y. Park, and A. Jacobi. Ceramics and ceramic matrix composites for heat exchangers in advanced
577 thermal systems—A review. *Applied Thermal Engineering*, 30(11-12):1277–1291, 2010.
- 578 [2] Paola Ranut. On the effective thermal conductivity of aluminum metal foams: Review and improvement of the available empirical and
579 analytical models. *Applied Thermal Engineering*, 101:496–524, May 2016.
- 580 [3] Rolf Landauer. The Electrical Resistance of Binary Metallic Mixtures. *Journal of Applied Physics*, 23(7):779–784, July 1952. ISSN
581 0021-8979, 1089-7550. doi: 10.1063/1.1702301.

- 582 [4] R. Coquard, D. Baillis, and E. Maire. Numerical investigation of the radiative properties of polymeric foams from tomographic images. *Journal of Thermophysics and Heat Transfer*, 24(3):647–658, 2010.
- 583 [5] R. Wulf, M. A. A. Mendes, V. Skibina, A. Al-Zoubi, D. Trimis, S. Ray, and U. Gross. Experimental and numerical determination of effective thermal conductivity of open cell fecral-alloy metal foams. *International Journal of Thermal Sciences*, 86:95–103, 2014.
- 584 [6] C. Y. Zhao, T. J. Lu, H. P. Hodson, and J. D. Jackson. The temperature dependence of effective thermal conductivity of open-celled steel alloy foams. *Materials Science and Engineering: A*, 367(1-2):123–131, February 2004. ISSN 09215093. doi: 10.1016/j.msea.2003.10.241.
- 585 [7] T. Fend, B. Hoffschmidt, R. Pitz-Paal, O. Reutter, and P. Rietbrock. Porous materials as open volumetric solar receivers: Experimental determination of thermophysical and heat transfer properties. *Energy*, 29(5-6):823–833, April 2004. ISSN 03605442. doi: 10.1016/S0360-5442(03)00188-9.
- 586 [8] R. Coquard, D. Rochais, and D. Baillis. Experimental investigations of the coupled conductive and radiative heat transfer in metallic/ceramic foams. *International Journal of Heat and Mass Transfer*, 52(21-22):4907–4918, October 2009. ISSN 00179310. doi: 10.1016/j.ijheatmasstransfer.2009.05.015.
- 587 [9] M. Tancrez and J. Taine. Direct identification of absorption and scattering coefficients and phase function of a porous medium by a Monte Carlo technique. *International Journal of Heat and Mass Transfer*, 47(2):373–383, January 2004. ISSN 00179310. doi: 10.1016/S0017-9310(03)00146-7.
- 588 [10] Simon Guévelou, Benoit Rousseau, Gilberto Domingues, Jérôme Vicente, and Cyril Caliot. Representative elementary volumes required to characterize the normal spectral emittance of silicon carbide foams used as volumetric solar absorbers. *International Journal of Heat and Mass Transfer*, 93:118–129, February 2016. ISSN 00179310. doi: 10.1016/j.ijheatmasstransfer.2015.09.069.
- 589 [11] M. Loretz, R. Coquard, D. Baillis, and E. Maire. Metallic foams: Radiative properties/comparison between different models. *Journal of Quantitative Spectroscopy and Radiative Transfer*, 109(1):16–27, 2008.
- 590 [12] T. J. Hendricks and J. R. Howell. Absorption/scattering coefficients and scattering phase functions in reticulated porous ceramics. *Journal of Heat Transfer*, 118(1):79–87, 1996.
- 591 [13] D. Baillis, M. Arduini-Schuster, and J-F. Sacadura. Identification of spectral radiative properties of polyurethane foam from hemispherical and bi-directional transmittance and reflectance measurements. In *ICHMT Digital Library Online*. Begel House Inc., 2001.
- 592 [14] M. A. A. Mendes, P. Talukdar, S. Ray, and D. Trimis. Detailed and simplified models for evaluation of effective thermal conductivity of open-cell porous foams at high temperatures in presence of thermal radiation. *International Journal of Heat and Mass Transfer*, 68:612–624, 2014.
- 593 [15] Gerard L Vignoles. A hybrid random walk method for the simulation of coupled conduction and linearized radiation transfer at local scale in porous media with opaque solid phases. *International Journal of Heat and Mass Transfer*, 93:707–719, 2016.
- 594 [16] R. Coquard and D. Baillis. Modeling of heat transfer in low-density eps foams. *Journal of heat transfer*, 128(6):538–549, 2006.
- 595 [17] M. A. A. Mendes, V. Skibina, P. Talukdar, R. Wulf, U. Gross, D. Trimis, and S. Ray. Experimental validation of simplified conduction–radiation models for evaluation of effective thermal conductivity of open-cell metal foams at high temperatures. *International Journal of Heat and Mass Transfer*, 78:112–120, 2014.
- 596 [18] R Coquard, D Baillis, and D Quenard. Experimental and theoretical study of the hot-wire method applied to low-density thermal insulators. *International journal of heat and mass transfer*, 49(23-24):4511–4524, 2006.
- 597 [19] M. Niezgodá, D. Rochais, F. Enguehard, P. Echegut, and B. Rousseau. Modeling of time-resolved coupled radiative and conductive heat transfer in multilayer semitransparent materials up to very high temperatures. *Applied Physics Letters*, 99(22):224101, 2011.
- 598 [20] Morgan Sans, Vincent Schick, Olivier Farges, and Gilles Parent. Experimental characterization of the coupled conductive and radiative heat transfer in ceramic foams at high temperature. *International Journal of Heat and Mass Transfer*, page article number 119077, 2020.
- 599 [21] V. M. Patel, M. A. A. Mendes, P. Talukdar, and S. Ray. Development of correlations for effective thermal conductivity of a tetrakaidecahedra structure in presence of combined conduction and radiation heat transfer. *International Journal of Heat and Mass Transfer*, 127:843–856, 2018.
- 600 [22] MA Badri, Pierre Jolivet, B Rousseau, Steven Le Corre, H Digonnet, and Y Favennec. Vectorial finite elements for solving the radiative transfer equation. *Journal of Quantitative Spectroscopy and Radiative Transfer*, 212:59–74, 2018.
- 601 [23] Richard Fournier, Stéphane Blanco, Vincent Eymet, Mouna El Hafi, and Christophe Spiesser. Radiative, conductive and convective heat-transfers in a single monte carlo algorithm. In *Journal of Physics: Conference Series*, volume 676, page 012007. IOP Publishing, 2016.
- 602 [24] Najda Villefranque, Richard Fournier, Fleur Couvreur, Stéphane Blanco, Céline Cornet, Vincent Eymet, Vincent Forest, and Jean-Marc Tregan. A path-tracing monte carlo library for 3-d radiative transfer in highly resolved cloudy atmospheres. *Journal of Advances in Modeling Earth Systems*, 11(8):2449–2473, 2019.
- 603 [25] Cyril Caliot, Stephane Blanco, Christophe Coustet, Mouna El-Hafi, Vincent Eymet, Vincent Forest, Richard Fournier, and Benjamin Piaud. Combined conductive-radiative heat transfer analysis in complex geometry using the monte carlo method. In *CTRPM-VI - 6th Computational Thermal Radiation in Participating Media VI, EURO THERM 110*, Cascais, Portugal, April 2018. URL <https://hal.archives-ouvertes.fr/hal-02096305>.
- 604 [26] L. Ibarrart, C. Caliot, M. El Hafi, R. Fournier, S. Blanco, S. Dutour, J. Dauchet, J-M. Tregan, V. Eymet, and V. Forest. Combined conductive-convective-radiative heat transfer in complex geometry using the monte carlo method : Application to solar receivers. In *International Heat Transfer Conference 16*, pages 8135–8142, Beijing, China, 2018. Begellhouse. doi: 10.1615/IHTC16.pma.023662.
- 605 [27] Léa Penazzi, Stéphane Blanco, Cyril Caliot, Christophe Coustet, Mouna El Hafi, Richard Fournier, Mathieu Galtier, Loris Ibarrart, and Maxime Roger. Toward the use of symbolic monte carlo for conduction-radiation coupling in complex geometries. In *Proceedings of the 9th International Symposium on Radiative Transfer, RAD-19*. Begel House Inc., 2019.
- 606 [28] J-M. Tregan, S. Blanco, C. Caliot, J. Dauchet, M. El Hafi, V. Eymet, R. Fournier, O. Farges, J. Gautrais, and M. Roger. Transient conducto-radiative heat transfer in a single monte-carlo algorithm: Handling the nonlinearity. In *Proceedings of the 9th International Symposium on Radiative Transfer, RAD-19*. Begel House Inc., 2019.
- 607 [29] Richard P Feynman, Albert R Hibbs, and Daniel F Styer. *Quantum mechanics and path integrals*. Courier Corporation, 2010.
- 608 [30] Mark Kac. On distributions of certain wiener functionals. *Transactions of the American Mathematical Society*, 65(1):1–13, 1949.
- 609 [31] A. Haji-Sheikh and E. M. Sparrow. The Floating Random Walk and Its Application to Monte Carlo Solutions of Heat Equations. *SIAM*

- 647 *Journal on Applied Mathematics*, 14(2):370–389, March 1966. ISSN 0036-1399, 1095-712X. doi: 10.1137/0114031. URL <http://epubs.siam.org/doi/10.1137/0114031>.
- 648
- 649 [32] Hammersley J. M. and Handscomb D. C. *Monte Carlo Methods*. Chapman and Hall, 1969.
- 650 [33] Denis Maillat. *Thermal quadrupoles: solving the heat equation through integral transforms*. John Wiley & Sons Inc, 2000.
- 651 [34] Jorge J Moré. The levenberg-marquardt algorithm: implementation and theory. In *Numerical analysis*, pages 105–116. Springer, 1978.
- 652 [35] Rémi Coquard, Denis Rochais, and Dominique Baillis. Conductive and radiative heat transfer in ceramic and metal foams at fire temperatures. *Fire technology*, 48(3):699–732, 2012.
- 653
- 654 [36] H Poltz and R Jugel. The thermal conductivity of liquids—iv: Temperature dependence of thermal conductivity. *International Journal of Heat and Mass Transfer*, 10(8):1075–1088, 1967.
- 655
- 656 [37] W. Pabst, E. Uhlířová, T. and Gregorová, and A. Wiegmann. Young’s modulus and thermal conductivity of closed-cell, open-cell and inverse ceramic foams—model-based predictions, cross-property predictions and numerical calculations. *Journal of the European Ceramic Society*, 38(6):2570–2578, 2018.
- 657
- 658 [38] Jun E Li and Baolin Wang. Equivalent thermal conductivity of open-cell ceramic foams at high temperatures. *International Journal of Thermophysics*, 35(1):105–122, 2014.
- 659
- 660 [39] Gerard L Vignoles and Alberto Ortona. Numerical study of effective heat conductivities of foams by coupled conduction and radiation. *International Journal of Thermal Sciences*, 109:270–278, 2016.
- 662

663 7. Appendices

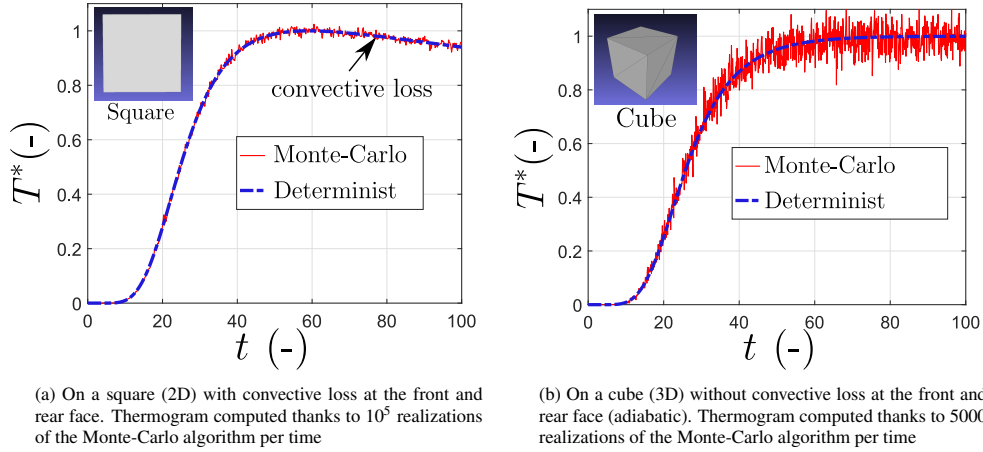


Figure 18: Comparison of the rear face thermograms on a Flash configuration computed with the Monte Carlo method and the finite element method (commercial software)

664 7.1. Purely conductive case: Flash configuration

665 For this first case, a purely conductive homogeneous solid medium (no radiation) was considered. A transient heat flux was applied on the front face such that:

666

$$\Phi(t) = Q \left(\mathcal{H}(t > 0) - \mathcal{H}(t - t_p > 0) \right) \quad (27)$$

667 with t_p the time duration of the excitation and Q the constant heat flux deposited. The parameters were set as $\lambda_s = 1$
 668 $\text{W} \cdot \text{m}^{-1} \cdot \text{K}^{-1}$, $\alpha = 1 \text{ mm}^2 \cdot \text{s}^{-1}$ and $t_p = 10 \text{ s}$. Studied geometries were simply a square and a cube whose sides had
 669 a length of 10 cm. fig. 18 shows thermograms computed with the described MC method and with the finite elements
 670 method (commercial software Flexpde®). A dimensionless temperature such as $T^* = (T_{\text{rt}}(t) - T_1)/(T_{\text{max}} - T_1)$ was
 671 introduced with T_{max} the maximum temperature of the thermogram.

672 In fig. 18(a), on a square 2D geometry, the thermogram was discretized in 1000 time intervals and 10^5 realizations of
 673 the MC algorithm were performed for each time value. Convective losses on the front and rear face were considered
 674 ($h = 5 \text{ W} \cdot \text{m}^{-2} \cdot \text{K}$) with a fluid temperature set to the initial temperature T_1 . The other boundaries were adiabatic.

675 Thus, the heat transfer was unidirectional. A good level of agreement was observed between the two methods and the
676 well-known shape of the rear face thermogram for the flash configuration was successfully obtained. In fig. 18(b), on
677 a cube 3D geometry, the thermogram was also discretized in 1000 time intervals but only 5000 realizations of the MC
678 algorithm were performed. Convective losses were removed so the system reached a new temperature equilibrium
679 at steady-state. In that case, a good level of agreement was also found between the two methods. Nevertheless, the
680 solution computed with the Monte-Carlo method appears noisier than in the previous case due to a low number of
681 realizations of the MC algorithm per time.

682 We would like to simply stress at this point the fact that the uncertainty associated with a MC computation is dependent
683 on the number of realizations performed. The solution computed by the Monte Carlo algorithm and its associated
684 error can be compared to the thermogram obtained by a measuring instrument. For the Monte Carlo algorithm, the
685 associated uncertainty simply depends on the number of paths followed and, therefore, on the calculation time. The
686 solution obtained by Monte Carlo tends towards the solution obtained by the deterministic solver with the increase
687 of the number of realizations. This noise is independent and centered on the solution which means it can be taken
688 into account during the inversion procedure (like during an experimental measurement) and implies an error in the
689 estimated parameters. It is therefore possible to reduce computation time with the present approach but with reduced
690 precision in the estimated parameters.

691 *7.2. Coupled conductive and radiative transfers: 1D Flash configuration, opaque parallel plates separated by void*
692 *phase*

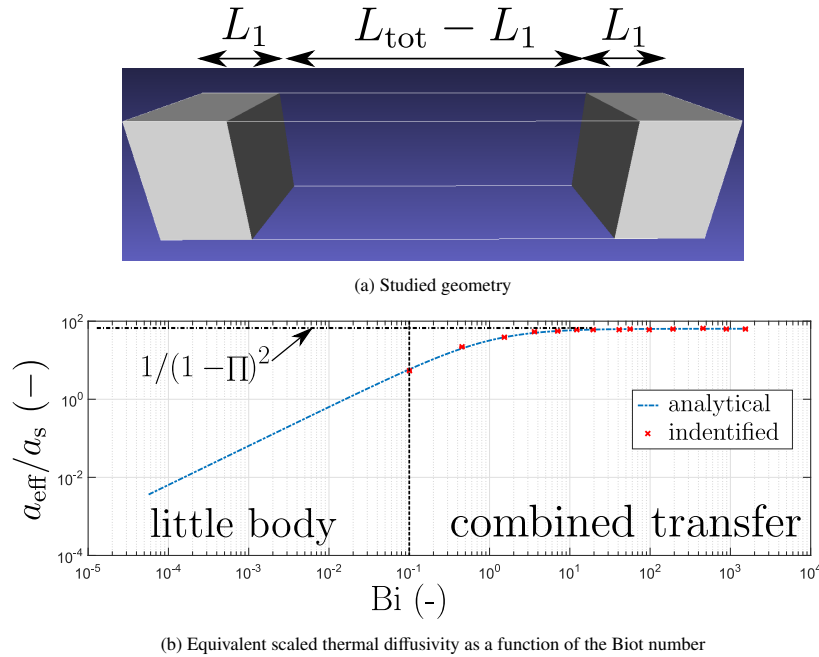


Figure 19: Comparison of the analytical solution and the solution estimated by inversion of the thermogram generated by MC

693 The previous example only dealt with the simple case of pure conduction in a homogeneous medium. The more
694 complex case of coupling between conduction and radiation is considered here. This academic case was studied by
695 Vignoles [15] to validate his coupled conductive and radiative stochastic method and to identify the equivalent thermal
696 diffusivity of foams [39]. The problem is defined by solid plates of thickness L_1 which are homogeneous, parallel
697 and opaque with a given emissivity ϵ . Each plate is separated by a void phase of thickness $L_{tot} - L_1$ and are assumed
698 infinite in the other two directions. Thus, the considered thermal problem is unidirectional.

699 This thermal problem has an analytical solution. By writing the balance of the conductive and radiative fluxes (cf.

700 eq. (9)) at the interface, the equivalent diffusivity between two separated plates can be written as:

$$\alpha_{\text{eff}} = \frac{\alpha_s}{(1 - \Pi)^2} \left(1 + \frac{2 - \epsilon}{Bi} \right)^{-1} \quad (28)$$

701 with α_{eff} the equivalent diffusivity, $\Pi = 1 - L_1/L_{\text{tot}}$ the volume fraction and Bi the radiative Biot number defined such
702 as:

$$Bi = \frac{h_{\text{rad}}L_1}{\lambda_s} = \frac{4\epsilon\sigma T_{\text{ref}}^3 L_1}{\lambda_s} \quad (29)$$

703 The simulation with the MC algorithm was performed on the geometry represented in fig. 19(a). The simulation of
704 the coupled heat transfer of the equivalent homogeneous medium was based on the quadrupole method [33], which is
705 very convenient for simulation of multi-layer and one dimensional heat transfer. A bi-layer medium was thus modeled.
706 The first layer was defined with a thermal diffusivity α_{eff} , which accounts for the first soleplate and the void phase
707 while the second, defined with α_s , accounts only for the second soleplate. The inverse procedure aims to identify the
708 value α_{eff} of the homogeneous model that allows the best match with the thermogram obtained with the 3D simulation
709 computed with MC.

710 In fig. 19(b), the estimated values of the equivalent diffusivity are represented as a function of the radiative Biot num-
711 ber for a given value of volume fraction Π . These values and their associated uncertainties are compared with the
712 analytical solution given in eq. (28). For $Bi > 0.1$, a good level of agreement was found between our estimated equiv-
713 alent diffusivity and the analytical solution. Given the associated uncertainty, the results are statistically compatible.
714 This means we can have great confidence in the described procedure involving direct modeling with combined MC
715 algorithm and inversion based on the use of a homogeneous equivalent model.

716 Computation with the MC algorithm becomes difficult in the case of a low radiative Biot number (little body assump-
717 tion $Bi < 0.1$) which constitutes a limit of the present MC algorithm. For low value of h_{rad} , the probability of a path
718 located at the boundary to jump through the void phase is very low and therefore many attempts are required to allow
719 a given path to reach the front face, location of thermal excitation. This means the computation time needed to build a
720 usable thermogram is increased too much. Convergence issues are highlighted even in this simple 1D case. Solutions
721 exist like the introduction of arbitrary probabilities but have not been considered in the case of the described MC
722 algorithm and could be the subject of further studies.